Flame resolved simulation of a turbulent premixed bluff-body burner experiment. Part I: Analysis of the reaction zone dynamics with tabulated chemistry

Fabian Proch[a,*], Pascale Domingo[b], Luc Vervisch[b], Andreas M. Kempf[a]

[a] *Chair of Fluid Dynamics, Institute for Combustion and Gasdynamics (IVG), University of Duisburg-Essen, 47048 Duisburg, Germany*
[b] *CORIA - CNRS, Normandie Université, INSA de Rouen, Technopole du Madrillet, BP 8, 76801 Saint-Etienne-du-Rouvray, France*

Abstract

Results from a highly resolved simulation are presented for a turbulent lean premixed methane-air bluff-body burner investigated experimentally at Cambridge University and Sandia National Laboratories. The Cartesian computational grid consists of 1.6 billion cells with a resolution of 100 µm, which is sufficient to capture the laminar (thermal) flame thickness of 500 µm. The combustion process is modeled with premixed flamelet generated manifolds (PFGM). The quality of the simulation is assessed by investigating the resolution of the flame- and velocity scales, it is demonstrated that the relevant scales are resolved in a direct numerical simulation (DNS) sense in the flame. The simulation is validated by comparing temporal statistics of velocity, temperature and major species mass fractions against experimental results. It is shown that the combustion regime varies with the distance from the burner and the progress of the reaction. Ensemble-averaged statistics, conditional means and averages along turbulent flamelets are compared against reference data from unstrained premixed one-dimensional flames. The analysis is carried out with respect to previous findings from DNS of much simpler flame configurations featuring synthetic turbulence.

*Corresponding author
Email address: fabian.proch@uni-due.de (Fabian Proch)

It is concluded that the major physical properties are comparable. In other words, most of the findings from previous DNS studies for canonical cases are relevant, at least for the lab-scale jet-flame examined here. The flame normal strain is found to be aligned with the most compressive strain rate. The mean principal curvature of the progress variable isosurfaces is predominantly zero and skewed towards positive values, the turbulent flame structure is mainly slightly thinned compared to the laminar one. The displacement speed of the flame is found to take partially negative values. The lack of correlation between the displacement speed and the consumption speed is also reported, the correlation being achieved considering the normal component of the diffusive flux only.
Keywords: Turbulent combustion, Direct numerical simulation, Tabulated chemistry, Premixed flames, Stratified flames

---

1. Introduction

Direct numerical simulations (DNS) have been used over the last decades to gain a deeper understanding of the governing physical mechanisms of turbulent combustion. DNS provides three-dimensional velocity and scalar fields, which are resolved in space and time. These results are useful to complement experimental observations and are also the key element in the development of combustion models for Reynolds-averaged Navier-Stokes simulations (RANS) and large eddy simulations (LES) – which will both be the only viable tools for the computation of technically relevant combustors in the foreseeable future. Recent overviews on the topic of combustion DNS are given by Chen [1] and by Poinsot and Veynante [2].

When focusing on premixed turbulent combustion, DNS simulations can be categorized in groups based on the complexity of the chemical mechanism, the type and strength of turbulence occurring, and the complexity of the geometry. A large amount of early and recent work was performed for planar or spherical flames interacting with canonical flow configurations, mostly either homogeneous turbulence or larger single vortices, with reduced chemical mechanisms

or tabulated chemistry [3–10], more detailed chemical mechanisms [11–13] or detailed chemical mechanisms [14].

Another group of direct numerical simulations deals with more complex slot- or Bunsen-flames, applying more detailed chemical mechanisms [15–19]. Although these configurations are more realistic than the canonical cases, they are still compact enough to resolve all flame- and velocity scales properly in a DNS sense.

Classically, combustion models can be developed based on DNS results of the aforementioned simplified flame configurations. Nevertheless, the turbulent flow structures in technically relevant burners are usually more complex than in these simplified configurations. It is therefore mandatory to validate the obtained models also in more realistic flame configurations, as occurring in lab-scale experiments. A classical DNS of these experiments would be computationally too expensive, therefore LES or RANS simulations are performed with the developed combustion models instead. The performance of the models is then judged by comparing (time-averaged) simulation results against experimental measurements. One serious issue with this approach is that, due to the complex interaction of sub-filter closures for the unresolved velocity scales and the sub-filter flame wrinkling, errors might compensate or amplify. Therefore, a clear and definitive judgment of the combustion model performance is hardly possible, which makes a further development of these models based on such comparisons questionable.

However, if the focus is on the development of sub-filter closures for models based on strongly reduced or tabulated chemistry, as they are applied in the vast majority of LES or RANS computations, flame resolved simulations are possible with the computational power available today. The saving of computational time with respect to a classical DNS has two major reasons. First, the chemical species that need to be transported for the strongly reduced or tabulated chemistry can be resolved on a significantly coarser grid than it is required for a more detailed chemical mechanism. Second, the Kolmogorov length scale increases significantly from the unburned to the burned side of the flame, due

to the increase in viscosity. As the main focus in the development of models for premixed combustion is on the influence of a given level of velocity fluctuations on the flame propagation, a slight under-resolution of the Kolmogorov scales in the fresh gases can be tolerated when full resolution of the signals is secured in the reaction zone. This kind of simulation has the potential to fill the gap in-between highly resolved 'classical DNS' for simpler configurations on the one hand, and LES (for real technical configurations) on the other hand, and may be termed as 'quasi DNS' or 'flame resolved simulation', where the latter term is chosen for the remainder of the paper. This new paradigm in turbulent flame simulation allows for comparing flame resolved simulation data against experiments and to carefully validate the simulated flow physics, as it has been done for 'classical DNS' of non-reactive flows for quite some years [20, 21]. The main advantage is that the lab-scale configurations considered enable a further validation of the simulations and the applied combustion models under much more realistic flow conditions, in which the unsteady motion develops according to real turbulent flow properties. Compare to 'classical DNS', an additional and essential validation step may thus be performed, in which it is verified that the statistical flow properties of the DNS fields agree well with experimental measurements.

The first flame resolved simulation for a lab-scale experiment was presented by Moureau et al. [22], it was performed with a finest grid resolution of 100 µm and tabulated chemistry for a lean premixed methane-air swirl burner, which has been previously investigated experimentally by Meier et al. [23]. The applied grid resolution was sufficient to resolve the progress variable field as well as the velocity field inside the relevant flame region. (A small amount of unresolved velocity scales were still present in the unburned gas close to the walls of the swirler, which were dissipated by the numerical scheme.) A good agreement between simulation and measurement data was demonstrated, the results were then used for developing the filtered laminar flame probability density function (FLF-PDF) modeling approach, in which the unresolved fluctuations of the progress variable are related to an explicit filtering operation applied to one-

dimensional flamelets.

In the present paper, a flame resolved simulation of a lab-scale flame is presented for a lean premixed methane-air bluff-body burner investigated experimentally at the University of Cambridge and the Sandia National Laboratories by Hochgreb and co-workers and Barlow and co-workers [24–29], and also numerically with LES by various groups [30–34]. In contrast to the work of Moureau et al. [22], the focus of the present paper lies on the analysis of the reaction zone dynamics and the turbulence-flame interaction based on the un-filtered progress variable and velocity fields, rather than on a-priori model development, a topic which is considered in a subsequent paper [35]. The goal is to analyze the flame resolved simulation results for a lab-scale burner with respect to the findings from previous DNS performed in much simpler configurations.

The details of the modeling and the experimental and numerical setup are described in the first section of the paper. Afterwards, a careful analysis of the resolution of flame- and velocity scales is presented and the statistically converged mean and rms profiles obtained from the simulation are compared against the available experimental data. Ensemble-averaged conditioned probability density functions (PDFs) and conditioned joint probability density functions (JPDFs) are then evaluated based on all available data points from the last time step of the simulation. It is shown that a conditioning on the height above the burner and the progress of reaction is necessary to obtain a maximum of information from the data. In the near burner region, the flame is only weakly affected by turbulence. This changes further downstream, due to the interaction of the reaction zone with the turbulence originating from the outer stream and the shear layer between the two streams. The correlations between the strain rate components and the progress variable field are investigated, where the focus is on the comparison with the reference laminar flame structure, used in topology-based subgrid-scale models. The progress variable field is characterized by its gradient, curvature and the local displacement speed of its iso-surfaces. Furthermore, various properties related to the reaction zones are extracted and examined for further analysis.

2. Premixed flame modeling

The goal of this work is to provide and investigate a database of a flame resolved simulation of a lab-scale burner experiment, which can be used for future validation and development of sub-filter closures for LES or RANS combustion models. Such LES or RANS computations are very often performed with tabulated chemistry, most of the reported LES studies for the investigated burner have been carried out with this approach [30–33]. Therefore, tabulated chemistry was also used for the quasi DNS, in order to enhance the comparability.

There are several strategies available for tabulating chemistry [36–39], in this work the premixed flamelet generated manifolds (PFGM) method was applied, which is described in detail by van Oijen and de Goey [40] and by van Oijen et al. [41] and was already used for the LES of the same burner [32]. The basis for the PFGM table are one-dimensional freely propagating laminar methane-air flames, which are computed with the Cantera library developed by Goodwin [42], using the GRI-3.0 mechanism by Smith et al. [43]. As the premixed methane-air streams mix with the air of the co-flow further downstream, flamelets have to be tabulated for the whole flammability range, in-between equivalence ratio values of 0.45 and 1.8. Outside the flammability limit, ideal mixing towards pure air or fuel at the lean or rich side was assumed, respectively. The resulting manifold was mapped onto a two-dimensional equidistant lookup table discretized in 201 entries in normalized progress variable direction and 1001 entries in mixture fraction direction.

A non-normalized progress variable was constructed from the sum of species mass fractions $Y_\mathrm{C} = Y_{\mathrm{CO_2}} + Y_\mathrm{CO} + Y_{\mathrm{H_2O}}$, which was applied with good success before in the LES of the same burner [32]. More complex fuels and rich mixture fraction conditions can require a more extensive progress variable definition, as presented by Ihme et al. [44], Niu et al. [45], Prüfert et al. [46] and others. The normalized progress variable value for the table-lookup is computed from:

$$C = \frac{Y_\mathrm{C} - Y_\mathrm{C}^\mathrm{min}(Z)}{Y_\mathrm{C}^\mathrm{max}(Z) - Y_\mathrm{C}^\mathrm{min}(Z)} \tag{1}$$

The mixture fraction Z is introduced following the definition by Bilger et al. [47]. In the fresh gas, it is linked to the equivalence ratio via:

$$\phi = \frac{Z}{1-Z}\frac{1-Z_s}{Z_s} \tag{2}$$

Here $Z_s = 0.054$ denotes the stoichiometric mixture fraction for methane-air. Overall, this tabulated chemistry behaves like a (hypothetical) single-step chemistry, which would be perfectly tuned to capture the flame speed, major species profiles and temperature.

The transport equations for progress variable and the mixture fraction solved during the quasi DNS-computation read:

$$\frac{\partial \rho Y_\mathrm{C}}{\partial t} + \frac{\partial}{\partial x_i}\left(\rho u_i Y_\mathrm{C}\right) = \frac{\partial}{\partial x_i}\left(\left[\rho D + \frac{\mu_t}{\mathrm{Sc}_t}\right]\frac{\partial Y_\mathrm{C}}{\partial x_i}\right) + \dot{\omega}_\mathrm{C} \tag{3}$$

$$\frac{\partial \rho Z}{\partial t} + \frac{\partial}{\partial x_i}\left(\rho u_i Z\right) = \frac{\partial}{\partial x_i}\left(\left[\rho D + \frac{\mu_t}{\mathrm{Sc}_t}\right]\frac{\partial Z}{\partial x_i}\right) \tag{4}$$

The turbulent viscosity is kept in the formulas with a turbulent Schmidt-number of $\mathrm{Sc}_t = 0.7$. It will be demonstrated in Section 4 that the sub-filter contribution is necessary in terms of numerics in the shear layers far upstream of the flame, whereas its overall contribution stays negligible in the vicinity and inside the flame zone, and therefore cannot alter the physics of the quantities examined in this work. The turbulent viscosity is computed based on the σ-model by Nicoud et al. [48], which was chosen as it predicts a viscosity of zero near walls and in expanding flows.

The diffusion coefficient was set to $D = \lambda/(\rho c_p)$ in Eqs. 3 and 4, as a Lewis number of unity was assumed for all species during the flamelet computations, which is a common practice in many turbulent flow simulations [e.g 49–52]. It is demonstrated in Fig. 1 that this assumption of a unity Lewis number has only a small influence on the propagation speed and thickness of a laminar methane-air flame for equivalence ratios smaller than $\phi = 0.75$, the maximum deviation is around 5% (a larger deviation is observed for richer mixtures that are not considered here). The heat conductivity and the heat capacity are denoted by λ and c_p, respectively. The resulting diffusion coefficient was stored together with

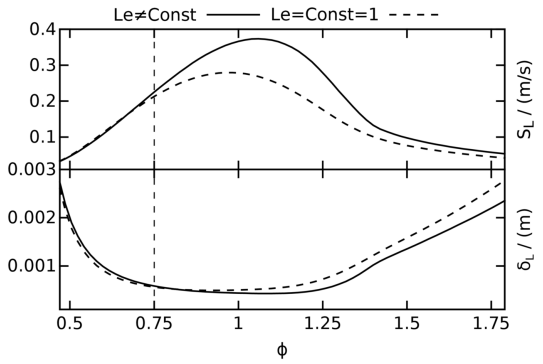

Figure 1: Laminar flame speed (top) and thickness (bottom) as a function of the equivalence ratio ϕ obtained from Cantera [42] freely propagating flame computations with the GRI-3.0 mechanism [43]. Compared are computations with individual Lewis numbers for all species (Le $\neq$ Const) and with a fixed Lewis number of unity for all species (Le = Const = 1). The present paper considers a ϕ range from 0 to 0.75.

the gas density ρ (which is needed for the applied incompressible or low-Mach number solution algorithm), the laminar viscosity μ and the progress variable source term $\dot{\omega}_C$ in the PFGM lookup table.

3. Experimental and numerical setup

The experimental setup of the investigated burner is presented in Fig. 2. The measurements have been carried out by Hochgreb and co-workers at the University of Cambridge and Barlow and co-workers at the Sandia National Laboratories [24–29]. The central bluff-body is surrounded by two co-annular premixed methane-air streams at ambient conditions, which are embedded in a co-flow of air with a velocity of 0.4 m/s. For further details please refer to Table 1.

Pseudo-turbulent fluctuations were imposed at the inlet, which were generated with the filtering method by Klein et al. [53] in an efficient numerical implementation [54]. A sensitivity study was performed on a reduced domain to find the parameters for the inflow-generator which result in the best agreement with the measured fluctuations at the first measurement position. It was found

that an integral lengthscale of $L = 0.5$ mm and a fluctuation level of 10% of the mean velocity, as given in Table 1, led to the best results. This integral lengthscale deviates from the ones measured by Zhou et al. [26], which were in between 2.4 mm and 3.9 mm. One possible explanation is that the imposed pseudo-turbulent fluctuations have only one integral lengthscale, whereas in reality there exists a broader and complex spectrum of flow scales at the inflow, spreading the kinetic energy over a wider variety of scales. We do, however, note that the lengthscales given by the experimentalists are very high in relation to the annular gaps (around 5 mm width, see Fig. 2). This may imply that the measured lengthscales rather represent some shedding at low frequencies induced by the geometry.

The laminar flame speed $S_L = 0.212$ m/s and flame thickness $\delta_L = 0.565$ mm were determined from the laminar flame computation for the equivalence ratio of $\phi = 0.75$. The flame thickness is based on the maximum temperature gradient and the temperatures in the unburned T_u and burned T_b gas:

$$\delta_L = \frac{T_b - T_u}{\max\left(\frac{dT}{dx}\right)} \tag{5}$$

The turbulent Reynolds number Re_T, Damköhler number Da and Kolmogorov lengthscale η_K were computed as follows, with the kinematic viscosity ν set to $1.6\,\mathrm{x}10^{-5}\,\mathrm{m}^2/\mathrm{s}^2$ and all other values taken from Table 1:

$$\mathrm{Re}_T = \frac{u' L}{\nu} \tag{6}$$

$$\mathrm{Da} = \frac{S_L L}{u' \delta_L} \tag{7}$$

$$\eta_K = L\,\mathrm{Re}_T^{-\frac{3}{4}} \tag{8}$$

The simulation was performed with the in-house code 'PsiPhi' that solves the governing equations in a low-Mach number finite-volume formulation, details can be found in previous publications by Kempf and co-workers [32, 55–59]. The spatial discretization relies on a central-differencing scheme for momentum and a total variation diminishing (TVD) scheme for the scalars, where the non-linear CHARM limiter [60] was applied. The solution is advanced in time with an

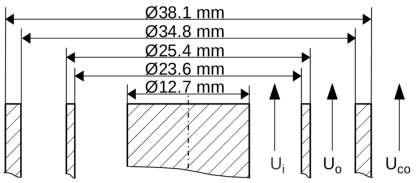

Figure 2: Sketch of the investigated burner setup.

Table 1: Boundary conditions and resulting turbulence-flame interaction parameters for the inner and outer stream.

Stream	u	u'	L	T	ϕ	Re	S_L	δ_L	Re_T	Da	η_K
	m/s	m/s	mm	K	-	-	m/s	mm	-	-	µm
Inner	8.31	0.9	0.5	295	0.75	5960	0.212	0.565	28.1	0.2	40.9
Outer	18.7	1.8	0.5	295	0.75	11,500	0.212	0.565	56.3	0.1	24.3

explicit low-storage third order Runge-Kutta scheme using a CFL number of 0.5. The geometry was described by an immersed boundary technique, continuity is ensured by a pressure correction method embedded in a predictor-corrector scheme. A successive over-relaxated Gauss-Seidel solver was applied for the solution of the Poisson-equation for the pressure. Around 80 iteration steps were necessary per Runge-Kutta sub-step to solve the Poisson equation with a maximum residual of 0.1 Pa, this consumed 35% of the total run time.

The code is parallelized using the distributed memory message passing interface (MPI), where non-blocking communication was used to overlay the communication with computation. The computational domain consisted of 1120x1200x1200 equidistant cells with an edge-length of 100 µm. The last 12 mm of the burner geometry were included into the computational domain as immersed boundaries. This led to a total amount of 1.6 billion control volumes. The computations were carried out on the Blue Gene/Q machine JUQUEEN at the Jülich Supercomputing Centre on 64,000 processor cores. The simulated physical time was 0.34 seconds corresponding to 195,000 time steps, which required a total amount of 10 million core hours.

4. Resolution of flame- and velocity scales

The sufficient resolution of the velocity scales on the computational grid is checked by two different measures, on the one one hand based on the estimated Kolmogorov length scales, and on the other hand based on the remaining turbulent viscosity as predicted from the σ-model. The level of resolution of the progress variable source term on the computational grid is addressed also, to conclude on the quality of the reaction zone description.

4.1. Kolmogorov length scales

The Kolmogrov length scale is computed as [61, 62]:

$$\eta_K = \left(\frac{\nu^3}{\epsilon}\right)^{1/4} \tag{9}$$

Here, ν denotes the kinematic viscosity and ϵ describes the rate at which the energy is transfered within the inertial subrange, it is approximated based on the integral lengthscale and the turbulent kinetic energy [61, 62]:

$$\epsilon \approx \frac{\overline{u'}^3}{L} \tag{10}$$

To compute the integral lengthscales and the velocity fluctuations, the data for all transported quantities in the burner mid-section, as shown in Fig. 12, has been collected for the last 240 statistical sample steps during the simulation. The turbulent velocity fluctuations have been evaluated by subtracting the time-averaged mean velocity fields (denoted by a bar operator) from the instantaneous velocity fields:

$$u_i'(t) = u_i(t) - \overline{u}_i \quad \text{with} \quad \overline{u}_i = \frac{1}{T}\int_{t=0}^{t=T} u_i(t)\mathrm{d}t \tag{11}$$

The averaged rms of all three velocity components was used for the computation of the turbulent kinetic energy:

$$\overline{u'} = \sqrt{\frac{1}{3}\overline{u_i' u_i'}} \tag{12}$$

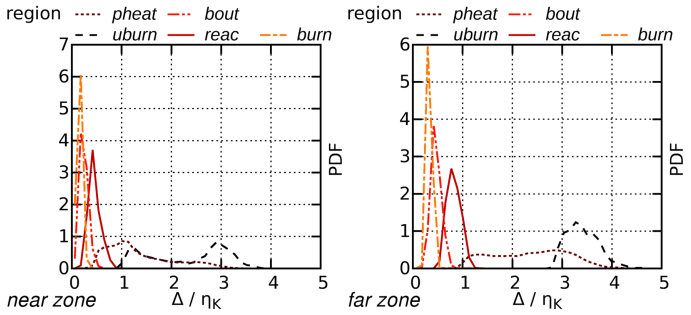

Figure 3: Ratio of the grid resolution to the Kolmogorov length scales. *The different plots show the conditioning on the height above the burner, whereas the different lines represent the conditioning on the progress of the reaction (see Section 4).*

The integral lengthscales were obtained from integration of the normalized time-averaged spatial auto-correlation function (summation convention not applied for greek letters):

$$L^{\pm}_{u_\alpha x_\alpha} = \int_{r=0}^{r=R^*} \frac{\overline{u'_\alpha\left(x_\alpha\right) u'_\alpha\left(x_\alpha \pm r\right)}}{\overline{u'_\alpha\left(x_\alpha\right) u'_\alpha\left(x_\alpha\right)}} \mathrm{d}r \tag{13}$$

The upper integration limit R^* is reached when the auto-correlation function either crosses zero or reaches a minimum. The lengthscale fields were smoothed by averaging over the positive and negative x- and y-direction:

$$L = \frac{1}{4}\left(L^+_{ux} + L^-_{ux} + L^+_{vy} + L^-_{vy}\right) \tag{14}$$

The resulting conditional PDFs of the ratio of the grid resolution to the Kolmogorov length scales are presented in Fig. 3. The PDFs are conditioned on the progress of the reaction, as usually done to assess turbulent premixed combustion [63]. The respective regions (with somewhat arbitrary definition) for conditioning are shown in the laminar flamelet for the inlet equivalence ratio of $\phi = 0.75$ in Fig. 4. The range $0.01 \leq \mathrm{C} < 0.02$ is considered as the unburned side of the flame, and is denoted *'uburn'*; $0.02 \leq \mathrm{C} < 0.6$ as the preheat zone is denoted *'pheat'*; $0.6 \leq \mathrm{C} < 0.8$ refers to the inner reaction zone, denoted *reac*, this zone was determined based on the species profile of the radical CH_3 (not shown in the plot); and $0.8 \leq \mathrm{C} < 0.98$ describes the burnout zone, denoted

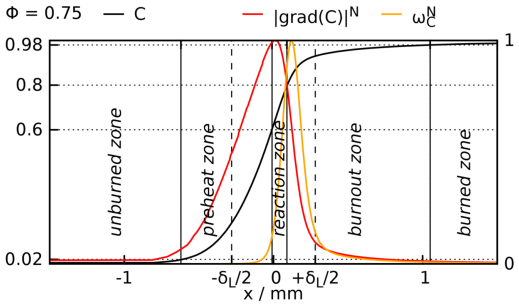

Figure 4: Laminar freely propagating flame for an equivalence ratio of $\phi = 0.75$. Plotted are the normalized progress variable C, the normalized progress variable gradient $|\mathrm{grad(C)}|^{\mathrm{N}}$ and the normalized progress variable source term $\dot{\omega}_{\mathrm{C}}^{\mathrm{N}}$. The different flame zones are separated by solid vertical lines. The range of the laminar flame thickness based on the thermal gradient centered at the location of maximum gradient of the progress variable C is marked by dashed vertical lines.

'bout'; finally $0.98 \leq \mathrm{C} < 0.99$ gives the burned side of the flame, which is denoted *'burn'*. The above regions were found to provide a useful conditioning of the PDFs, yielding greater insights. Furthermore, the PDFs are shown for two regions, the *near* region up to 35mm above the burner and the *far* region, from 35mm to 70mm above the burner. This conditioning on the height above the burner reflects the fact that the flame will interact with strong turbulence in the far zone only, as can be seen in Fig. 12.

The ratio of the grid resolution to the Kolmogorov length scale in Fig. 3 is a common measure for the resolution of a DNS, as discussed e.g. by Moin and Mahesh [20]. For the reaction zone, which is of high importance for the correct flame propagation, the ratio of the grid resolution to the Kolmogorov length scale is below unity for the vast majority of points, which indicates that all velocity scales are resolved. For the unburned- and preheat region, the ratio of the grid resolution to the Kolmogorov length scale reaches values up to four. According to Moin and Mahesh [20], this resolution might be sufficient for a classical DNS of homogeneous turbulence with a higher-order spectral code. With the applied second-order scheme, this means that a certain small amount of unresolved velocity scales is left in the unburned- and preheat region.

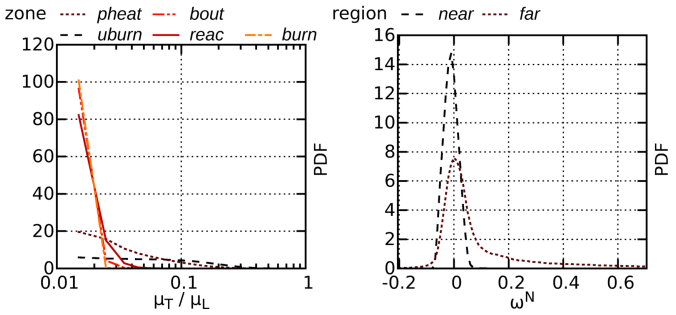

Figure 5:

Left: PDFs of the ratio of turbulent to laminar viscosity (due to the logarithmic abscissa the area below the PDFs is not unity). *The different lines represent the conditioning on the progress of the reaction (see Section 4).*

Right: Progress variable source term integrated in C-space over the turbulent flamelets normalized by the exact one-dimensional laminar results (see Eq. (15)). *The different lines represent the conditioning on the height above the burner (see Section 4).*

4.2. Ratio of turbulent to laminar viscosity

The potential influence of these remaining unresolved velocity scales in the unburned- and preheat region on the flame propagation is assessed by the ratio of turbulent viscosity resulting from the σ-model to the laminar viscosity. Figure 5 presents the conditional PDFs of the viscosity ratio, where the data points within the co-flow were omitted to not bias the unburned gas PDF towards zero, as the co-flow points have zero turbulent viscosity. (These points were detected by an axial velocity component smaller than 1 m/s and a radius larger than 14 mm.)

A clear dependence of the viscosity ratio on the progress of the reaction can be seen in Fig. 5. In the inner reaction zone, the burnout zone and at the burned side of the flame, the viscosity ratio takes negligible values. In the preheat zone, at more than 80% of the points the viscosity ratio is below 0.1, which means that the diffusive flux due to unresolved velocity scales is at most 10% of the laminar diffusive flux. Just on the unburned side of the flame, the viscosity ratio can take slightly larger values, but also stays well below 0.4. It can be summarized that the influence of the unresolved scales stays very moderate on

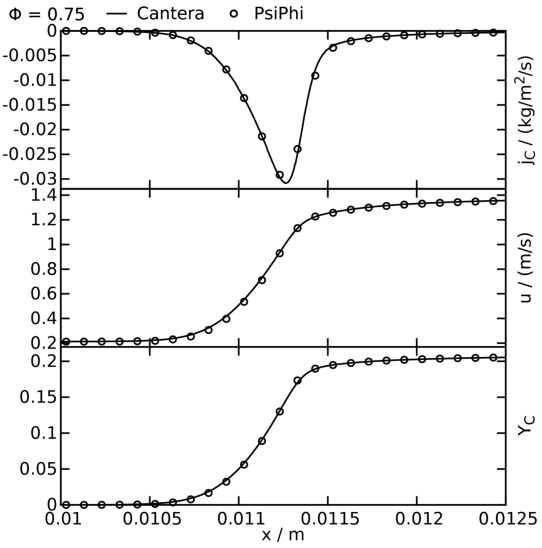

Figure 6: Comparison of a one-dimensional laminar freely propagating flame computed with Cantera [42] (lines) and the 'PsiPhi' code (one circle per cell, grid resolution of 100 µm) with a Lewis number of unity for all species for an equivalence ratio ϕ of 0.75. Shown are the profiles of the progress variable (bottom), the velocity (middle) and the diffusive flux of the progress variable $j_k = -\lambda/(\mathrm{Le}\, c_p)\, \partial Y_k/\partial x$ (top).

the unburned side of the flame and gets negligible inside the reaction zone on which the following investigations will focus.

4.3. Resolution of the progress variable field

The second point that needs to be demonstrated is whether the resolution of the progress variable field on the computational grid is sufficient. It is shown in Fig. 6 that the 'PsiPhi' code is able to predict a one-dimensional laminar freely propagating flame in good agreement with the Cantera reference solution on the applied grid resolution, the TVD scheme does not alter the diffusive fluxes. To assess the resolution of the turbulent flame, the structure of the local diffusive and reactive layers has been extracted from the simulation results. This was done by starting at all points that were located on the inner reaction zone iso-surface of $C = 0.83$, where the progress variable source term is largest, and moving for each of these points along the positive (respectively negative) local

flame normal direction, until a value of $C = 0.01$ (respectively 0.99) was reached. Local distributions that were not strictly monotonic in progress variable were discarded, we did not check for potential intersections of individual distributions. That way, roughly 0.8 million individual distributions across reaction zones, named thereafter as 'flamelets', were extracted for the further analysis.

To judge the resolution of the flamelets, it was exploited that the source term $\dot{\omega}_C$ for a given mixture fraction is an unambiguous function of the progress variable C in the applied tabulated chemistry approach. Therefore, the integration of the source term along the turbulent flamelets in C-space should always yield the same result as in a properly resolved one-dimensional laminar flame when the spatial resolution of the progress variable field is sufficient. Figure 5 shows the PDFs of the normalized deviation of the integrated source term of the turbulent flamelets from the integrated source term of the properly resolved one-dimensional flame for the average mixture fraction of the turbulent flamelets (the dependency on the mixture fraction Z is omitted for clarity):

$$\omega^{\mathrm{N}} = \frac{\int_{C=0.01}^{C=0.99} \dot{\omega}_{\mathrm{C}} \, \mathrm{d}C|_T - \int_{C=0.01}^{C=0.99} \dot{\omega}_{\mathrm{C}} \, \mathrm{d}C\big|_R}{\int_{C=0.01}^{C=0.99} \dot{\omega}_{\mathrm{C}} \, \mathrm{d}C\big|_R} \tag{15}$$

A value of $\omega^{\mathrm{N}} = 0$ corresponds to a perfectly resolved source term for one individual flamelet. It can be seen in Fig. 5 that in most of the flow locations the source term is nearly perfectly resolved. In the near region, the integration error due to the lack of resolution is below 5% for 70% of the flamelets, and the maximum error stays well below 10%. For the far region, the PDF of the resolved source term is still below 10% error for more than 75% of the points, but has a long tail towards positive deviations in the far region. An explanation for this is the occurrence of stratified regions further downstream, due to mixing with the co-flow air. The principal alignment of flame normal and mixture fraction gradient is such that the flame propagates towards a leaner mixture, which is termed as back-supported stratification, Cruz et al. [64] and Nguyen et al. [39] have shown that this leads to an increase of the flame propagation speed for lean conditions - which also comes along with a higher value of the source term

integral.

It can be summarized that inside the flame zone, which is the region of interest for the further analysis, the flame and velocity scales are resolved. A certain amount of unresolved velocity scales can still be found in the fresh gas. This means that the turbulent structures entering the flame zone might be influenced by a small degree, but that the interaction between turbulence and flame is fully resolved.

5. Comparisons of time-averaged statistics against measurements

To check the validity of the modeling approach and the general quality of the simulation results, statistical quantities (mean and rms) along sample lines are compared against experimental measurements. The sampling was started after 0.34 seconds, which corresponds to more than one flow-through time with respect to the co-flow velocity of 0.4 m/s. The sampling was carried out for another 0.14 seconds, which corresponds to more than 10 flow-through times with respect to the mean inner stream velocity of 8.31 m/s. It has been found in the preceding LES study of the same burner [32] that this sampling time was sufficient to obtain properly sampled statistics. The respective comparison against the LDA-measurements by Zhou et al. [26] (velocities) and the Raman/Rayleigh-measurements by Sweeney et al. [24] (temperature and species) are presented in Figs. 7 - 11 for heights of 10, 30, 50 and 70 mm above the burner exit. In general, a satisfactory agreement is found for all quantities for both mean and rms that is mostly better than in the previous LES studies of the same burner [30–34].

The comparison for the mean axial velocity component are presented in Fig. 7, it is over predicted at the centerline by the simulation at the first measurement position. This indicates that the strength of the recirculation zone in the region above the bluff-body is still under predicted, as it was already the case with LES [30, 32]. This could potentially be attributed to a minor influence of heat loss at the bluff-body in that region, which was shown in the LES of Mercier et al. [33]. However, this effect is limited to the small region above

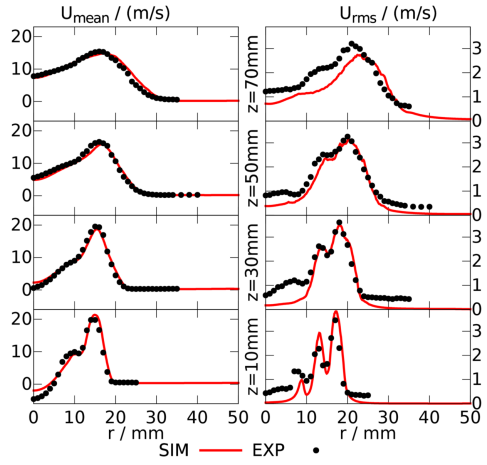

Figure 7: Comparison of mean and fluctuation profiles of the axial velocity component at different axial positions against experimental data [26].

the bluff-body and does not influence much the flame dynamics and the good agreement for larger radii and further downstream. At the last measurement position, the mean axial velocity profile is shifted slightly towards larger radii in comparison with the experiment, which corresponds to the simultaneously occurring shift of the mean temperature profile in Fig. 9 towards larger radii. Towards the centerline, the simulated velocity components are lower than in the measurements. As this behavior can also be observed in the co-flow region, where the fluctuations should be negligible, the observed deviation might at least partially be attributed to measurement noise. A notable feature of the rms axial velocity profiles is the small peak at a radius of approximately 8 mm. Whereas this flow feature had no big influence in the previously performed LES of the burner [32], the magnitude of the fluctuations at this position turned out to be of great importance for the correct flame shape and position at the first measurement position in the presented quasi DNS.

The agreement for the rms of the radial velocity component in Fig. 8 is very similar to the agreement for the rms of the axial velocity component. In contrast, larger deviations are found for the mean radial velocity component. Whereas the simulation results revert to zero at the centerline (as it should be the case

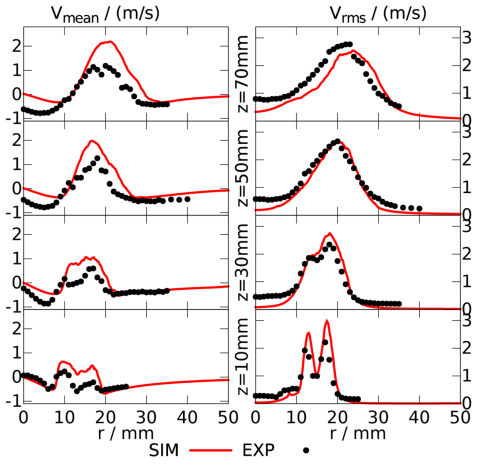

Figure 8: Comparison of mean and fluctuation profiles of the radial velocity component at different axial positions against experimental data [26].

in an axial-symmetric configuration), the measured results show a remaining radial velocity component. As burner geometries like the one investigated are known to be sensitive against minute deviations of the geometry, the actually measured flow field might indeed have been slightly asymmetric - which of course is not reproduced by the three-dimensional symmetric simulation setup. Near the bluff-body, where also the measured radial velocity component goes back to zero, a slight over-prediction of the radial velocity component by the simulation can be observed.

At 50 mm, both the mean and rms temperature profiles in Fig. 9 show a small shift towards larger radii compared to the experimental values. The thickness of the mean flame brush and the rms profile is under predicted by the simulation at 30 mm.

The mean equivalence ratio profiles in Fig 10 are shifted slightly towards larger radii in the simulation, which corresponds to the shift in the axial velocity component (Fig. 7) and the temperature (Fig. 9). The rms of equivalence ratio is under predicted at the last measurement position and towards the centerline, where the latter deviation may be related to measurement noise in the experiment. A conspicuous feature of the measured mean equivalence ratio pro-

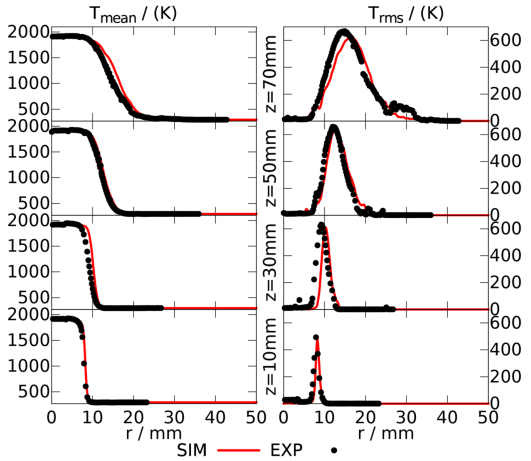

Figure 9: Comparison of mean and fluctuation profiles of the temperature at different axial positions against experimental data [24].

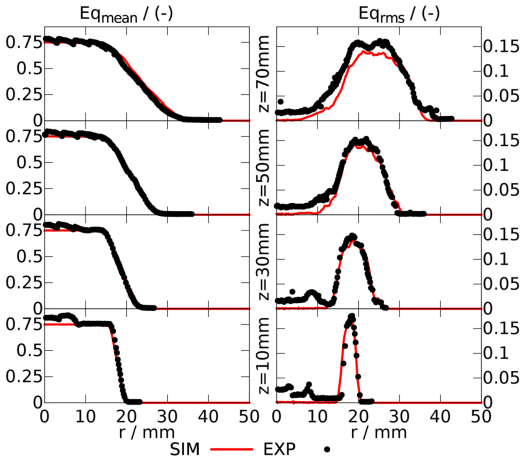

Figure 10: Comparison of mean and fluctuation profiles of the equivalence ratio at different axial positions against experimental data [24].

files is the kink towards the centerline near the bluff-body, which is not showing up at all in the simulation. According to Barlow et al. [65], this kink can be attributed to preferential transport of the major species CO_2 and H_2O as well as of the intermediate species CO and H_2. It was shown by Nambully et al. [30] that this phenomenon can be reproduced by solving an additional transport equation for the residence time of mixture fraction, although the obtained 'differential diffusion' mixture fraction was only used for post-processing. Nambully et al. [30] also discussed how the observation of differential diffusion on the mixture fraction is strongly influenced by the choice of the species to build the mixture fraction from the measurements.

To further assess the predictive capability of the tabulated chemistry approach, Fig. 11 presents a comparison between simulation and measurement for the intermediate species CO. The agreement of the mean CO profile in the flame zone is good, but the thickness of the burnout zone is under predicted by the simulation which leads to a faster decline of the mean CO value to zero towards the centerline than in the experiment. This can partially be attributed to the under-prediction of the mean temperature profile thickness at 30 mm in Fig. 9, another reason might be the Lewis number of unity assumption applied in the computation of the PFGM table. Corresponding to the observations made for the mean profiles, the rms profiles of CO also agree better within the flame region than in the burnout zone.

Overall, one can conclude that the simulation provides a good representation of the actual experiments. The large amount of additional information available in the database is now probed for deeper analysis of the ongoing physical phenomena.

6. Analysis of the turbulent flame structure

This section presents a detailed analysis of the turbulence-flame interaction in the investigated lab-scale burner, with respect to the findings from DNS of much simpler flow configurations. The main focus is on the comparison of the

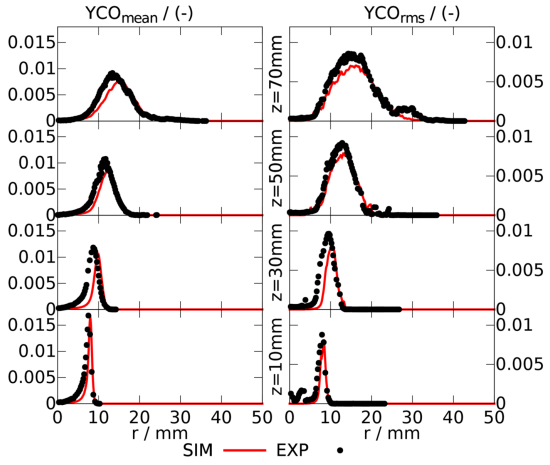

Figure 11: Comparison of mean and fluctuation profiles of CO at different axial positions against experimental data [24].

resulting turbulent flame structure to the laminar one, to progress in the context of flamelet-like sub-grid scale modeling. The first step is a phenomenological analysis of the flame structure based on instantaneous two-dimensional and three-dimensional contour plots. Afterwards, the combustion process is characterized with regime diagrams, and the interaction between turbulence and flame is investigated by conditional PDFs and joint PDFs of the strain rate component fields and the curvature, gradient and propagation speed of the flame. To the best of our knowledge, this is the first time that this kind of DNS analysis is applied to a dataset devoted to a lab-scale burner, after extensively validating the results against experimental measurements.

6.1. Two-dimensional instantaneous contour plots

For a first impression of the flow and scalar fields, Fig. 12 shows instantaneous contour plots of different quantities in the mid-section of the burner. The flow field illustrated by the velocity components in axial (U), radial (V) and circumferential (W) direction is determined by the interaction between the faster outer and the slower inner stream, the bluff-body and the flame. In the near-burner region, the flow field is dominated by the recirculation zone above

the bluff-body, which stabilizes the flame and is indicated by negative values of the axial velocity. The dilatation due to the temperature increase in the flame induces an additional radial velocity component, compared to non-reactive simulations and measurements of the investigated burner [26, 66, 67], which pushes the slower inner stream towards the faster outer stream and reduces the strength and length of the recirculation zone. Turbulent fluctuations are produced in the shear layers between the inner and outer stream, and between the outer stream and the co-flow. A large amount of the turbulent fluctuations is dissipated in the burned region (towards the centerline) due to the increase in viscosity caused by the temperature increase.

Because of the higher fluctuation level in the outer jet, the equivalence ratio field is getting wrinkled immediately after the burner exit. Turbulent mixing occurs in the mixing layer between the premixed streams and the air co-flow, which grows in thickness when moving downstream.

In contrast to the equivalence ratio field, the temperature field shows a relatively constant thickness of the interface between fresh and burned gas. This is due to the reaction source term, which counteracts the diffusion and steepens the reaction zone.

The flame front is indicated by the reaction source term of the progress variable. The flame is not influenced by strong turbulent fluctuations in the near region, where it is only moderately wrinkled. Things change in the far region, where the flame front gets wrinkled more strongly. Fresh gas starts penetrating into the burned region, this results in unburned mixture fingers as described in previous works [68–71]. Also the opposite phenomenon can be observed, when narrow regions of burned gas penetrate into the fresh gas, which further downstream leads to regions where pockets of burned gas exist in the fresh gas and regions where fresh gas is surrounded by burned gas in the burner mid-section.

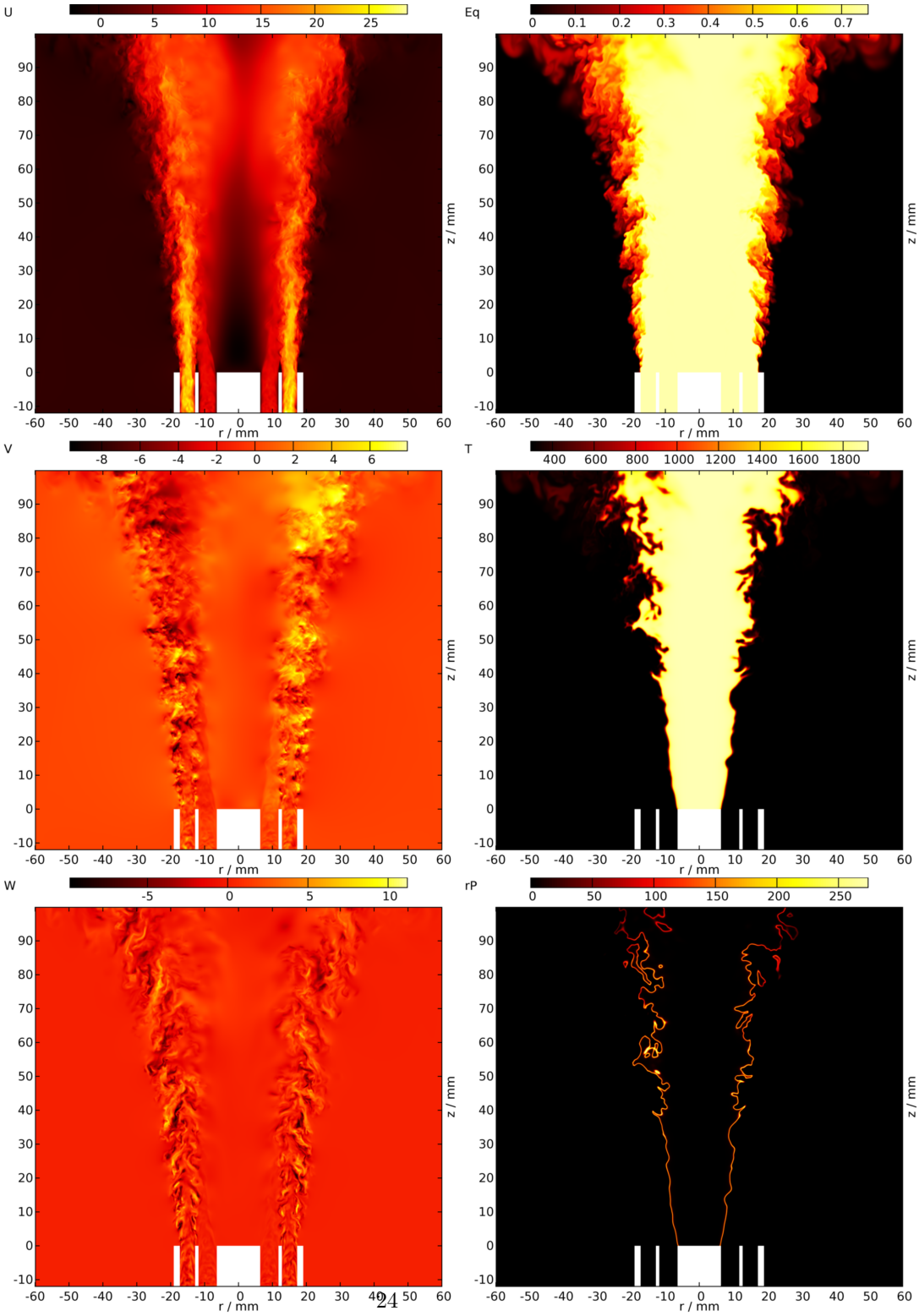

Figure 12: Contour plots in the burner mid-section of the axial (U), radial (V) and circumferential (W) velocity component, the equivalence ratio (Eq), the temperature (T) and the reaction source term of the progress variable (rP).

6.2. Three-dimensional instantaneous visualization

To get a better understanding of the overall flame structure, Fig. 13 presents the three-dimensional iso-surface for a progress variable value of 0.5, which is superimposed on the contour plot of equivalence ration. Immediately after the burner exit in the near region, the flame front develops surface-wave patterns with a relatively constant amplitude that are aligned parallel to the flow direction. When moving downstream in the far region, these structures get less aligned with the axial direction and develop varying amplitudes. No Kelvin-Helmholtz rollers, as in the equivalence ratio distribution, are formed in the progress variable field, as the shedding frequency of the bluff body (12.7 mm diameter) is significantly smaller than the shedding frequency of the outer tube (1.65 mm wall thickness). As already observed in the two-dimensional burner mid section plots in Fig. 12, when moving downstream in the far region, the flame surface gets more and more corrugated and develops deep valleys and high peaks. The pockets of burned gas surrounded by fresh gas, observed in the two-dimensional burner mid-section plots (Fig. 12), are also visible in the three-dimensional plot, most obviously far downstream. However, there seems to be no regions where fresh gas is completely surrounded by burned gas in the three-dimensional plot. Therefore, the areas of fresh gas surrounded by burned gas observed in the two-dimensional burner mid-section plots shown in Fig. 12 may actually be just cuts through deep unburned mixture fingers pointing in the circumferential direction.

6.3. Temporal development of scalar quantities

To gain further insight into the interaction between turbulence, combustion and mixing, Fig. 14 shows contour plots of the circumferential velocity component for two different time steps. The two time steps are separated by 172 µs, which corresponds to the sampling interval for the statistics of 100 computational steps. Applying Taylor's hypothesis, this time difference corresponds to roughly three integral time scales with respect to the inner stream mean velocity

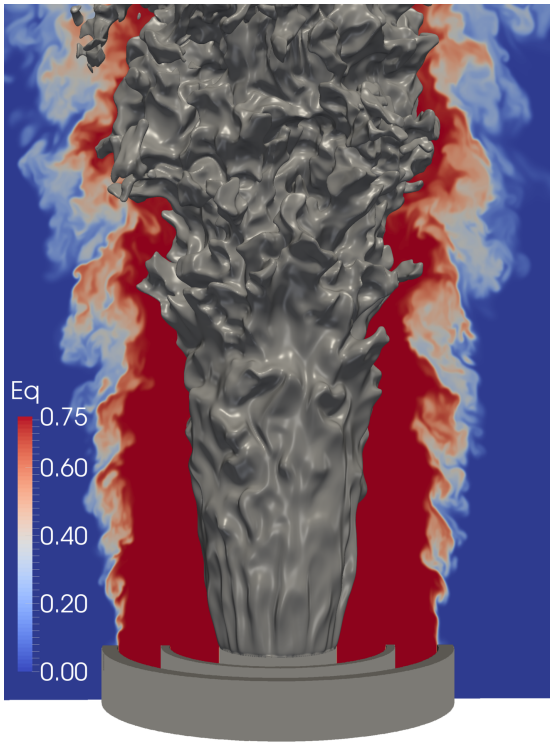

Figure 13: Contour plot of equivalence ratio in the burner mid-section, superimposed is an iso-surface for a progress variable value of $C = 0.5$.

of 8.31 m/s. As the investigated case is unswirled, the time-averaged circumferential velocity component is equal to zero, and therefore the instantaneous circumferential velocity directly gives the instantaneous circumferential velocity fluctuations. The flame position is represented by the red iso-line, which corresponds to a dimensionless progress variable value of $C = 0.5$. The mixing field is visualized by the white and the blue iso-line. The white iso-line represents the beginning of the mixing zone, to get a properly defined iso-line an equivalence ratio $\phi = 0.74$ is chosen, which is close to the $\phi = 0.75$ from the burner. The blue iso-line corresponds to the lean flammability limit of the methane-air mixture at $\phi = 0.45$, where the flame extinguishes.

In the near region, the flame is interacting with the velocity fluctuations originating from the inner stream. In the far region, the flame is exposed to the higher level of velocity fluctuations, originating from the outer stream and the shear layer between the inner and outer stream. The flame dampens the velocity fluctuations on the burned side significantly compared to non-reactive simulations and measurements of the investigated burner [26, 66, 67], and most of the turbulent structures are dissipated away.

Not only the structure of the flame in the two plots, but also the temporal change between the two plots is strongly affected by the level of turbulence. Whereas the flame shape is mainly shifted downstream in the near region, in the far region the flame shape is not only shifted, but also changed and deformed. Distinct features of the flame front are marked by circles in Fig. 14. The numbering and diameter of the circles in the plots is consistent, so that the structures can be compared.

Regions where burned mixture penetrates into the fresh gas are found to grow (1) and shrink (4) in thickness and depth. Pockets of fresh (burned) gas in burned (unburned) mixture can appear relatively rapidly, where this comes along with high magnitudes of circumferential velocity fluctuations, so that this actually seems to be due to the convection of three-dimensional structures into the mid-section (2 + 5).

The growth of pockets of fresh gas in burned mixture seems to come along

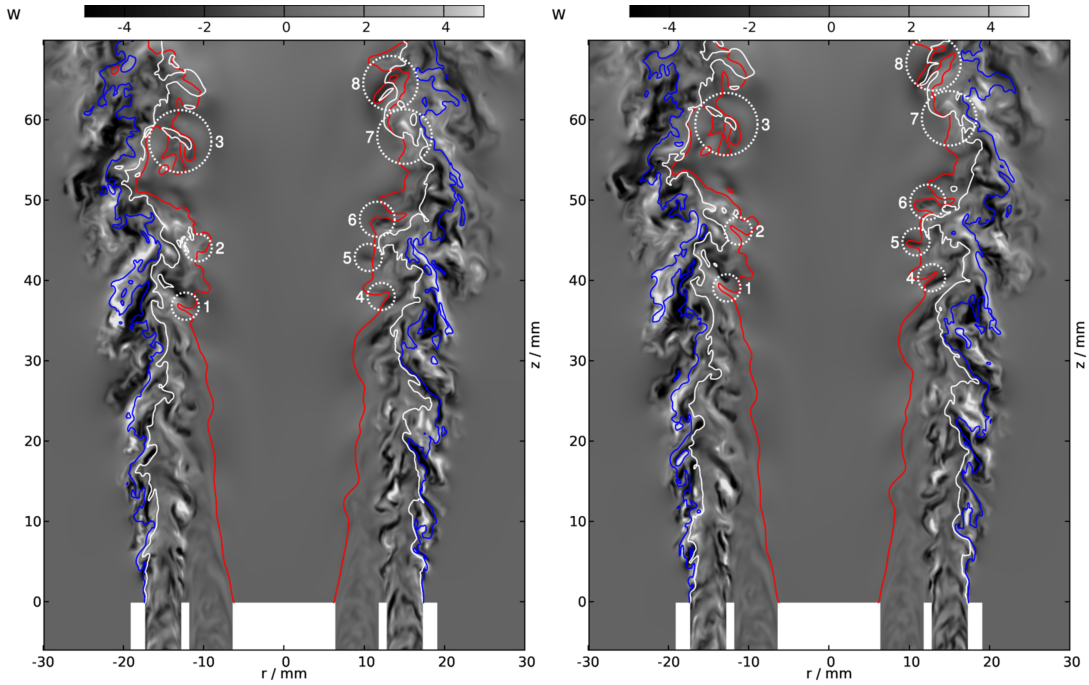

Figure 14: Interaction of turbulence, flame and mixing at two different time steps which have a temporal distance of 172 µs in the burner mid-section. Shown are the contour plots of the circumferential velocity component (W) superimposed with isolines for $C = 0.5$ (red), Eq = 0.74 (white) and Eq = 0.45 (blue), where the latter represents the lean flammability limit. Distinct features of the flame front are marked by circles, the numbering and diameter of the individual circles is the same in both plots.

with a narrowing of the 'neck' of the pocket (6), which leads to complex pocket structures further downstream (3). Regions where fresh gas is completely surrounded by burned gas can merge with the fresh gas side of the flame (8). As already discussed for Fig. 13, these seem to show cuts through fingers of unburned mixture, which are moved into the mid-plane by convection due to the high magnitude of circumferential velocity in these regions (8).

Regions of locally stratified combustion are found further downstream, where the flame wrinkling does not seem to be altered significantly, whereas the wrinkling of the mixture fraction iso-surface is strongly affected by the damping of turbulent fluctuations by the flame (7).

6.4. Combustion regime diagrams

To characterize the interaction between turbulence and combustion, the combustion regime diagrams according to Borghi [72] and Peters [61] are usually drawn. For the generation of these diagrams, the turbulent velocity fluctuations and the integral lengthscales in the burner mid-section, as described in Section 4, have been normalized by the time-averaged laminar flame speed and the time-averaged laminar flame thickness, respectively:

$$\frac{\overline{u'}}{\overline{S_L(Z)}} \tag{16}$$

$$\frac{L}{\overline{\delta_L(Z)}} \tag{17}$$

The resulting regime diagrams are shown in Fig. 15. The conditioning was done on the height above the burner and the progress of the reaction, as above. To clarify to which extent the smallest scales in the unburned gas are actually able to penetrate into the reaction zone and how the turbulence level is altered by the flame, the regime diagrams are shown for all zones of the flame.

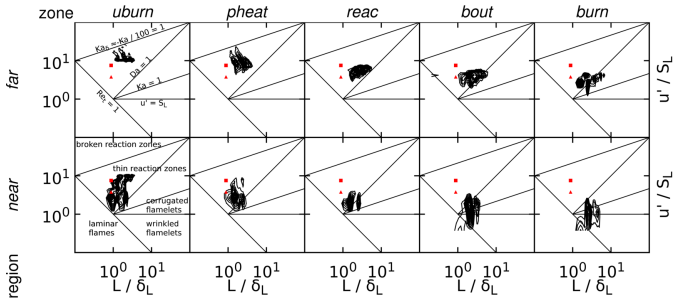

Figure 15: Combustion regime diagrams as suggested by Borghi [72] and Peters [61] with the conditioned joint PDFs of the velocity fluctuations normalized by the laminar flame speed (see Eq. 16) as a function of the integral lengthscale of the velocity fluctuations normalized by the laminar flame thickness (see Eq. 17). The inlet conditions for the inner and outer stream as given in Table 1 are marked by triangles and squares, respectively. *The different plots represent the conditioning on increasing height above the burner from bottom to top and increasing progress of the reaction from left to right (see Section 4).*

The diagrams for the unburned side of the flame indicate that the combustion process in the burner takes place in the thin reaction zone regime.

However, with increasing progress of reaction, the locations of the JPDFs are shifted significantly towards the corrugated flamelets regime due to a reduction of the normalized velocity fluctuations and an increase of the normalized integral length scales. The increase of the integral lengthscales means that the small unresolved scales that are present in the fresh gas are not able to penetrate into the reaction zone, and thus have limited influence on the combustion process, as it has also been discussed for the DNS of a canonical flow in the thin reaction zone regime, first by Poinsot et al. [5] and more recently by Poludnenko and Oran [69, 70]. This is also a potential explanation why flamelet-based models are frequently found to work well for flames outside the corrugated and wrinkled flamelet regime – at least if the location in the regime diagram is calculated based on the unburned gas turbulence.

The JPDFs in Fig. 15 are multimodal, which shows that multiple sources of turbulent fluctuations exist in the investigated burner, which result in a broad turbulent spectrum. First, the two inlet streams supply two different levels of (artificially generated) turbulence as shown in Table 1. Second, the shear at the bluff body, between the inner and outer stream and between the outer stream and the co-flow produces additional turbulent fluctuations, where the magnitude of the latter two exceeds the inflow turbulence level, as it can be seen in the radial fluctuation profiles in Figs. 7 and 8. Far downstream, some further increase of the normalized velocity fluctuations and a decrease of the normalized lengthscales can occur in the fresh gases, due to the reduction of the mixture fraction towards leaner values caused by mixing with the co-flow air, which reduces the laminar flame speed and increases the laminar flame thickness. It should however be stressed that the influence of stratification is only very weak in the investigated burner setup. With growing distance from the burner, the induced turbulent fluctuations and integral lengthscales are decreased and increased by molecular friction, respectively. The broad range of varying fluctuation levels distinguishes the investigated burner from canonical flow configurations, which isolate a single set of flow parameters. This confirms that the presented flame resolved simulation of a lab-scale burner is an interesting and challenging test

case for combustion models.

6.5. Strain rate components in the flame-aligned coordinate system

The turbulence induced strain rate determines the production of flame wrinkling and therefore is a key quantity in the analysis of the local flame structure [73–78].

For a closer analysis, the strain rate contributions in flame normal direction a_n and tangential to the flame front a_t are examined [2, 61]:

$$a_n = n_i n_j \frac{1}{2}\left(\frac{\partial u_i}{\partial x_j} + \frac{\partial u_j}{\partial x_i}\right) = n_i n_j \frac{\partial u_i}{\partial x_j} \tag{18}$$

$$\begin{aligned} a_t &= (\delta_{ij} - n_i n_j)\,\frac{1}{2}\left(\frac{\partial u_i}{\partial x_j} + \frac{\partial u_j}{\partial x_i}\right) \\ &= (\delta_{ij} - n_i n_j)\,\frac{\partial u_i}{\partial x_j} = -\left(a_n - \frac{\partial u_k}{\partial x_k}\right) \end{aligned} \tag{19}$$

The flame normal vector points into the fresh gas and is determined from:

$$\vec{n} = -\frac{\nabla Y_\mathrm{C}}{|\nabla Y_\mathrm{C}|} \tag{20}$$

A compressive strain rate component in flame normal direction is denoted by negative values, an expansive one by positive values. The last RHS expression in Eq. 19 expresses that the flame tangential strain rate is just the negative value of the flame normal strain rate with the velocity divergence subtracted.

6.5.1. Conditioned PDFs of the strain rate components

The PDFs of the described strain rate components conditioned on the progress of reaction and the axial position are shown in Fig. 16. At the unburned side of the flame, the flame normal strain rate component PDF is skewed towards negative values, i.e. there exists a compressive strain rate normal to the flame front. Furthermore, the PDF is broader in the more turbulent far region compared to the near region. In the burned gas, the PDF is less wide and symmetric than in the fresh gas. This can be explained by the significant increase of viscosity due to the temperature increase in the flame, which enlarges the diffusive flux

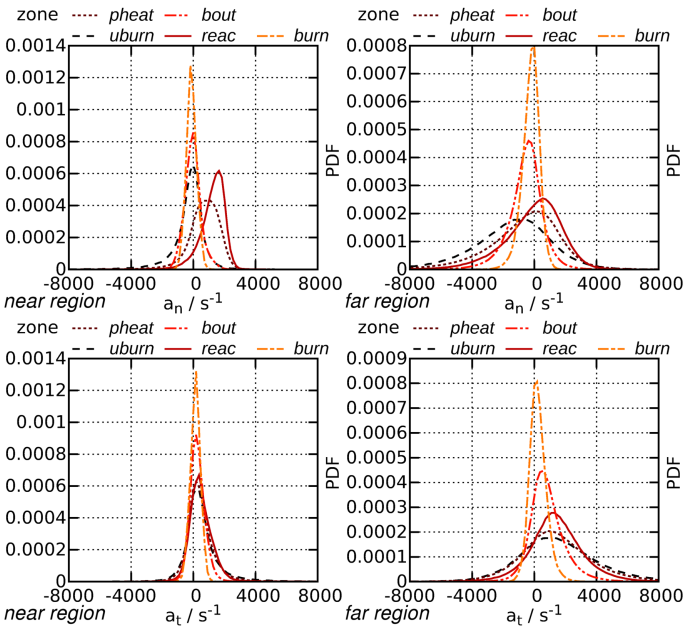

Figure 16: Conditioned PDFs of the strain rate component normal (top, see Eq. 18) and tangential (bottom, see Eq. 19) to the flame front. *The different plots show the conditioning on the height above the burner, whereas the different lines represent the conditioning on the progress of the reaction (see Section 4).*

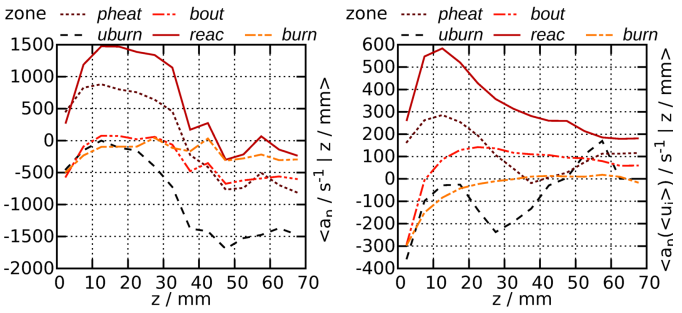

Figure 17: Conditional mean of the strain rate component normal to the flame front (see Eq. 18) as a function of the distance from the burner exit. The left plot shows the results for the whole three-dimensional instantaneous field, the right for the time-averaged field in the burner mid-section. *The different lines represent the conditioning on the progress of the reaction (see Section 4).*

and thereby reduces large strain rates. The mean of the flame normal strain rate component gets shifted towards positive values in the reaction zone due to dilatation.

In the PDFs of the tangential strain rate, most of the dilatation has been removed, therefore the positions of the PDF peak values for the different flame zones are nearly identical in the near region. The PDFs are skewed towards positive values in the unburned gas. Towards the burned side, the PDFs get significantly more symmetric, i.e. larger absolute values of tangential strain rate are reduced more. This is plausible as the strength of the molecular friction is proportional to the magnitude of the strain rate. In the far region the PDFs are much broader, and the peak values are shifted towards zero from the unburned to the burned side of the flame.

To investigate the reason for the observed skewness of the normal strain rate PDFs towards negative values at the unburned and burned side of the flame in the far region, Fig. 17 presents the conditional means of the flame normal strain rate, depending on the axial position and the progress of reaction. The left plot shows the conditional mean for the strain rate computed from the instantaneous velocity field in the last time step. (It must be stressed that due to the larger

number of sample points and the rotationally symmetric setup, the resulting conditional mean is nearly identical for different time steps.) For the conditional mean in the right plot, the strain rate was computed for the time-averaged velocity field in the burner mid-section. (The operator <|zone> represents the average over all points conditioned on the dimensionless progress variable, the operator <> the time-averaging.) The time-averaged conditional mean (right) results represent the general flow configuration determined by the flame position, the burner geometry and the mean inlet velocity profiles. The instantaneous conditional mean (left) results are a combination of the time-averaged strain rate and the strain rate due to turbulent velocity fluctuations. In the near region, the instantaneous conditional mean in the unburned gas is dominated by the time-averaged contribution. In the far region, the strain rate due to turbulence outweighs the time-averaged strain rate. The turbulence induced flame normal strain rate in the unburned gas takes negative values throughout the domain, the reason for this can be found in the alignment of the strain rate eigenvectors with the flame normal vector, a point that is now discussed.

6.5.2. Alignment statistics of the strain rate components and the flame normal vector

The alignment of the principal directions of the strain rate tensor with flame normal direction determines the evolution of scalar gradients and has been investigated before, based on simulation results [75, 79, 80] as well as on experimental measurements [81–83]. Figure 18 presents the conditional PDFs of the dot product of the flame normal vector with the most compressive and most extensive principal strain rate eigenvectors (the closer the dot product is to unity, the stronger is the alignment).

For the near region, the alignment PDFs in the unburned gas have a peak value at around 0.7 for both principal strain rate components, which corresponds to an angle of roughly 45° and is caused by the flow structures originated from the friction at the annular gap walls and in the shear layers. In the preheat, reaction and burnout zones, the flame induced extensive strain reduces

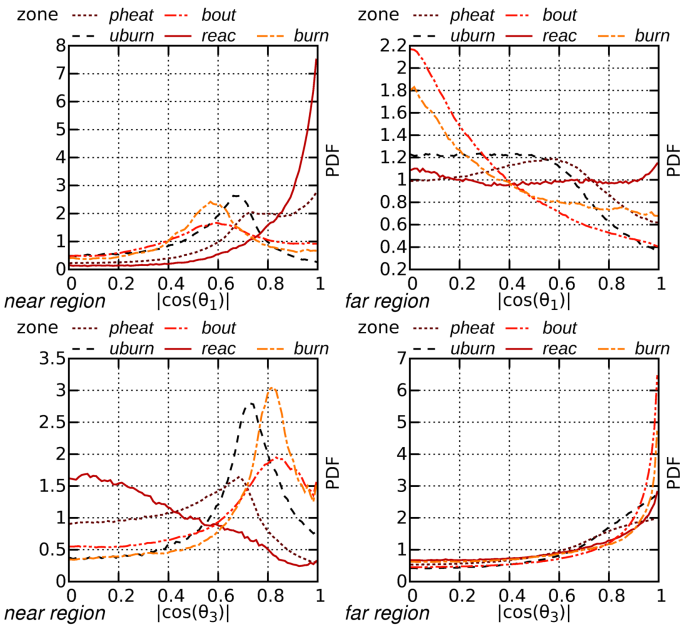

Figure 18: Conditioned PDFs of the alignment angle between the eigenvectors belonging to the most extensive (Θ_1, top) and the most compressive (Θ_3, bottom) principal strain rate and the flame normal vector. *The different plots show the conditioning on the height above the burner, whereas the different lines represent the conditioning on the progress of the reaction (see Section 4).*

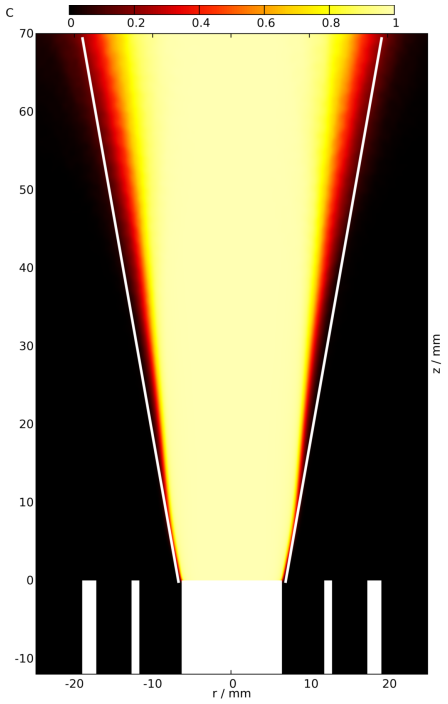

Figure 19: Time-averaged dimensionless progress variable contours in the burner mid section, the approximate mean flame brush angle of 10° against the vertical direction is marked by white lines.

the alignment with the most compressive strain rate eigenvector, in agreement with previous findings [e.g. 79, 81]. At the unburned side of the flame, the predominant alignment is again with the most compressive strain rate eigenvector, where the peak value has changed to around 0.83, corresponding to a shift by the approximate opening angle of the mean flame brush of 10° illustrated in Fig. 19.

For the far region, the alignment is predominantly with the most compressive strain rate eigenvector in the unburned gas, due to the stronger flame wrinkling and the large contribution of turbulence induced strain, which has been reported before for both non-premixed and premixed combustion [e.g. 75, 79, 82–84]. As in the near region, the alignment with the most compressive strain rate eigenvector weakens inside the reaction zone because of the flame induced extensive

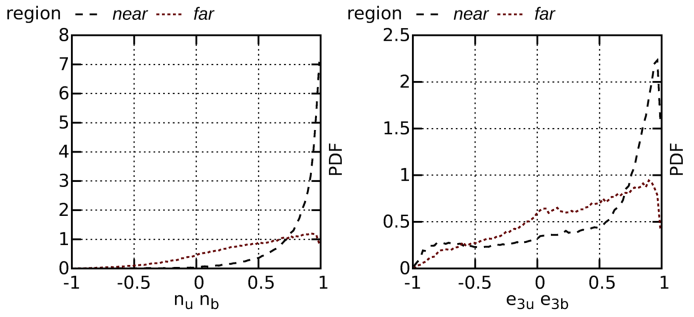

Figure 20: Conditioned PDFs of the aligment between the unburned and burned side of the flamelets. The left plot shows the respective alignment for the flame normal vector, the right plot for the most compressive strain rate eigenvector. *The different lines represent the conditioning on the height above the burner (see Section 4).*

strain and gets stronger again at the burned side of the flame.

Figure 20 shows the conditional PDFs of the dot product of the most compressive principal strain rate eigenvector as well as of the flame normal vector at the unburned and burned side of the extracted flamelets (see Section 4). In general, the change in direction is larger for the compressive strain rate eigenvector than for the flame normal vector. Especially in the near region, the compressive strain rate eigenvector alignment PDF has a distinct peak at a value that corresponds to roughly the opening angle of the mean flame brush (approximately 10°, see Fig. 19), whereas the most likely flame normal vector alignment is zero degree (corresponding to a value of unity in the plots). In the far region, there is a broader range of alignments also for the flame normal vector, which is however still much narrower than the range for the compressive strain rate eigenvector alignment. These observations indicate that the increased alignment of the flame normal vector with the most compressive strain rate eigenvector at the burned side of the flame compared to the unburned side seems to be mainly due to a change in the strain rate eigenvector direction, whereas the flame normal vector direction stays relatively unaffected throughout the flame.

6.6. Mean principal curvature of the progress variable field

The degree of flame surface wrinkling mainly determines the turbulent flame propagation speed for flamelet based combustion models, it can be measured by the mean principal curvature of the progress variable field ('mean' refers to the average of the principal curvatures and must not be confused with a temporal mean):

$$\kappa_m = \frac{1}{2}\frac{\partial n_i}{\partial x_i} \tag{21}$$

Positive (negative) values of the mean principal curvature connote that the flame front is convex (concave) towards the fresh gas, e.g. if a sphere of products (reactants) is surrounded by reactants (products). The spatial distribution of curvature and its importance for the turbulent flame propagation has been discussed in various previous works using DNS database of much simpler configurations [13, 15, 74, 76, 77, 85–87].

Figure 21 presents the PDFs of the mean principal curvature conditioned on the progress of reaction and the height above the burner. The PDFs are significantly broader in the far region in comparison to the near region, this can be explained by the higher turbulent fluctuation level further downstream, which causes stronger flame wrinkling. The PDFs are symmetric with respect to zero and bell-shaped in the fresh gas, which corresponds to the PDF shape of the turbulent velocity fluctuations that is typically Gaussian-like. With increasing progress of reaction, the PDFs get narrower and skewed towards positive values in the flame, the peaks are slightly shifted towards negative values. Similar shapes of the curvature PDFs were previously reported in the literature [15, 76, 77, 85, 87].

The narrowing of the curvature PDFs with increasing progress of reaction can mainly be attributed to the increase of the diffusivity and viscosity inside the flame due to the temperature rise. The increased diffusivity amplifies the diffusive fluxes mainly in strongly curved regions and thereby reduces large absolute values of curvature. The increased viscosity reduces the turbulent ve-

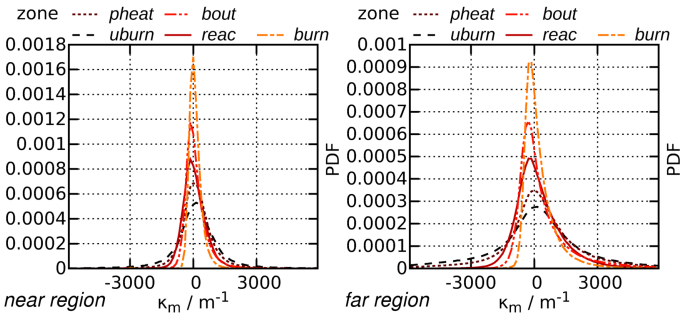

Figure 21: Conditioned PDFs of the mean principal curvature of the flame front (see Eq. 21). *The different plots show the conditioning on the height above the burner, whereas the different lines represent the conditioning on the progress of the reaction (see Section 4).*

locity fluctuations, which is reflected by the aforementioned reduction of the width and of the peak value of the PDF of the tangential strain rate component with increasing progress of reaction in Fig. 16. Figure 22 shows the JPDFs of the strain rate tangential to the flame and the mean principal curvature, a weak negative correlation is found, which is most significantly in the reaction zone and has also been observed in previous DNS of canonical flow configurations [3, 76, 78, 80, 88]. An increase (decrease) of tangential strain rate is related to a decrease (increase) of mean principal curvature. Therefore, the observed skewness of the mean principal curvature PDFs towards positive values, which increases with the progress of reaction, can be attributed to the shift of the peak values of the tangential strain rate PDFs in Fig. 16 towards smaller values inside the flame. Moreover, the reduction of the width of the tangential strain rate PDFs in the flame further reduces the width of the mean principal curvature PDFs.

6.7. Gradient of the progress variable field

Besides the already discussed mean principal curvature of the progress variable field, the second quantity with influence on the turbulent flame speed in flamelet based combustion models is the local gradient of the progress variable field, which has been discussed at many occasions before [10, 13, 15, 63, 79,

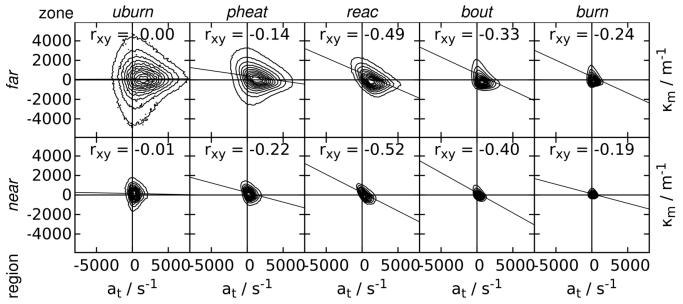

Figure 22: Conditioned joint PDFs of the mean principal curvature of the flame front (see Eq. 21) as a function of the strain rate component tangential to the flame (bottom, see Eq. 19). *The different plots represent the conditioning on increasing height above the burner from bottom to top and increasing progress of the reaction from left to right (see Section 4). The Pearson correlation coefficients* $\mathrm{r_{xy}}$ *and linear regression lines are also given.*

89, 90]. To judge the deviation of the local gradient of the turbulent progress variable field from the gradient in the respective one-dimensional laminar flame for the local values of the dimensionless progress variable C and the mixture fraction Z, the following normalized difference is used (the dependency on C and Z is omitted for clarity):

$$|\nabla Y_C|^{\mathrm{N}} = \frac{|\nabla Y_C| - |\nabla Y_C|_L}{|\nabla Y_C|_L} \tag{22}$$

The normalized gradient difference is zero in a laminar flame, positive (negative) values indicate a thinned (thickened) turbulent flame structure, with respect to the laminar flame. The minimum possible value is -1, which corresponds to an absolute gradient value of zero in the turbulent flame.

Figure 23 shows the PDFs of the normalized gradient difference conditioned on the progress of reaction and the height above the burner. In contrast to the observations made for the PDFs of the mean principal curvature in the last section, the width of the PDFs of the normalized gradient difference depends on the local heat release rate rather than on the progress of the reaction, i.e. the PDFs are most narrow in the inner reaction zone and get broader in both the fresh and the burned gas. This indicates that the inner reaction zone, which is

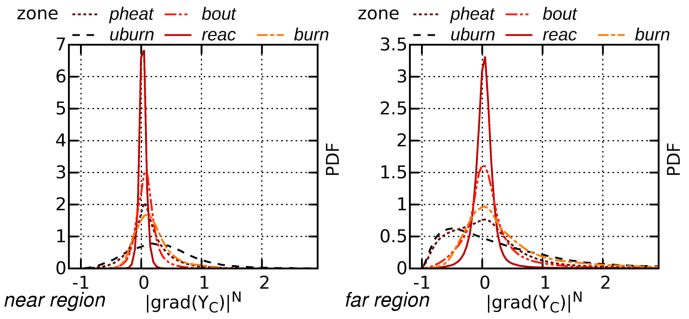

Figure 23: Conditioned PDFs of the difference of the absolute value of the normalized gradient difference of the turbulent and the laminar flame (see Eq. 22). *The different plots show the conditioning on the height above the burner, whereas the different lines represent the conditioning on the progress of the reaction (see Section 4).*

most important for the overall flame propagation as most of the heat is released here, has a structure that is close to the laminar flamelet and therefore can be described well by a flamelet-like modeling approach.

Except for the unburned side of the flame in the far region, the peaks of the PDFs are slightly shifted towards positive values which corresponds to a slightly thinner flame structure than the laminar one. The reason for the thinner flame structure can be found in the already discussed positive peak values of the tangential strain rate component PDFs in Fig. 16. As shown in Fig. 24, the correlation of the normalized gradient difference and the strain rate component tangential to the flame is positive everywhere in the domain, which corresponds to a negative correlation with the flame normal strain rate component that is in line with the classical theory and previous findings [63, 79, 80, 91]. The strength of the correlation increases from the unburned to the burned side of the flame, which implies that the effect of strain on the gradient becomes more significant the less the flame is wrinkled.

The thickening of the flame structure at the unburned side in the far region has also been reported before [63, 79, 80, 91] and can be explained by the already discussed predominant reduction of negative curvature values in the flame, as it can be seen in Fig. 21. This tends to reduce the flame propagation speed with

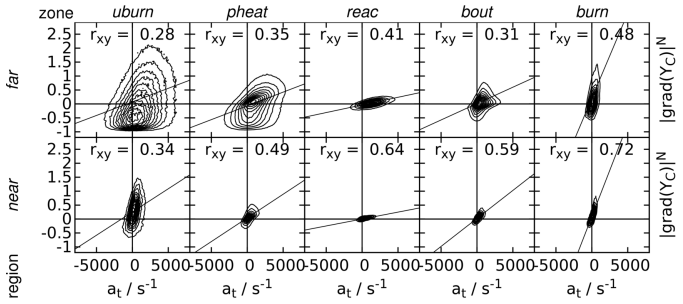

Figure 24: Conditioned joint PDFs of the normalized gradient difference of the turbulent and the laminar flame (see Eq. 22) as a function of the strain rate component tangential to the flame (see Eq. 19). *The different plots represent the conditioning on increasing height above the burner from bottom to top and increasing progress of the reaction from left to right (see Section 4). The Pearson correlation coefficients* $\mathrm{r_{xy}}$ *and linear regression lines are also given.*

increasing progress of reaction, which decreases the gradient of the progress variable as shown by Sankaran et al. [15].

In general, the peaks of the PDFs of the normalized gradient difference $|\nabla Y_C|^{\mathrm{N}}$ in Fig. 23 are located close to zero, which means that it is most likely to have the same gradient as in a laminar flame. This implies that the laminar flame structure is the stable solution of Eq. 3. This makes sense as the source term and the diffusion coefficient obtained from the PFGM-table are always identical to that in the laminar flame. This means that the main difference between the turbulent and laminar flame is a mean principal curvature unequal to zero. The most likely value for the mean principal curvature is approximately zero, as it can be seen in Fig. 21, thus the most likely flame structure should be very close, at least on average, to the laminar one.

To investigate the turbulent flame structure in more detail, the tortuosity τ of the extracted flamelets (see Section 4) has been determined:

$$\tau = \frac{L_f}{D_f} \tag{23}$$

Here, D_f denotes the shortest distance between the start and end point of the flamelet at $C = 0.01$ and $C = 0.99$, respectively. The distance between the start and end point of the flamelet when moving along the local flame normal direction

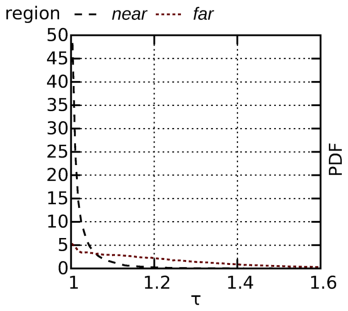

Figure 25: Conditioned PDFs of the tortuosity of the flamelets (see Eq. 23). *The different lines represent the conditioning on the height above the burner (see Section 4).*

is given by L_f. Figure 25 shows the conditioned PDFs of the tortuosity, a value of unity corresponds to a straight line and a value of infinity would correspond to a circle. The larger the tortuosity is, the more the respective flamelet deviates from a straight line. In the near region, approximately one third of the flamelets are 'perfectly' straight lines, the longest flamelets that are found are less than 20% longer than a straight line (corresponding to $\tau = 1.2$). In the far region, the flamelets are much more wrinkled and deviate more significantly from a straight line, values up to 1.6 are found for the tortuosity. This corresponds to the findings of Poludnenko and Oran [69], who observe that the turbulent flame structure consists of tightly folded flamelets for a canonical flame configuration in the thin reaction zone combustion regime.

6.8. Flame displacement speed

The flame displacement speed is the speed at which an isoline would propagate relatively to the flow, it reflects the local flux balance between convective fluxes, diffusive fluxes and reaction source term. It is computed from the following equation based on the non-normalized progress variable Y_C [92–94]:

$$\begin{aligned} S_d &= \frac{\nabla \cdot (\rho D \nabla Y_\mathrm{C}) + \dot{\omega}_\mathrm{C}}{\rho \left|\nabla Y_\mathrm{C}\right|} \\ &= \frac{\overbrace{\vec{N} \cdot \nabla \left(\rho D \vec{N} \cdot \nabla Y_\mathrm{C}\right)}^{S_n} \overbrace{-2\rho D_\mathrm{C}\, \kappa_m \left|\nabla Y_\mathrm{C}\right|}^{S_t} \overbrace{+\dot{\omega}_\mathrm{C}}^{S_r}}{\rho \left|\nabla Y_\mathrm{C}\right|} \end{aligned} \tag{24}$$

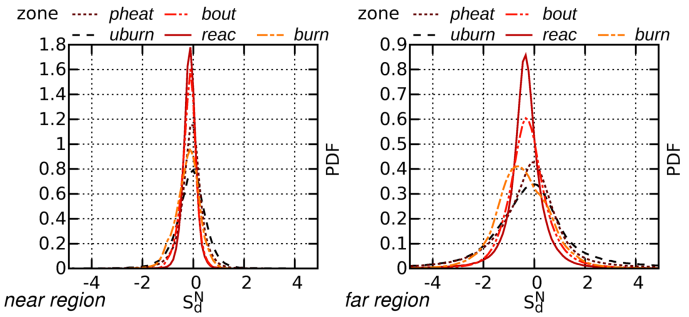

Figure 26: Conditioned PDFs of the normalized deviation of the displacement speed of the flame front from the laminar flame speed (see Eq. 25). *The different plots show the conditioning on the height above the burner, whereas the different lines represent the conditioning on the progress of the reaction (see Section 4).*

The contributions of the flame normal diffusion component, the diffusion due to the mean principal curvature (which is zero in a planar flame) and the chemical source term are denoted by S_n, S_t and S_r, respectively. As the focus in this work is on the comparison with the laminar flame, in the further analysis the normalized deviation of the displacement speed from the laminar flame speed for the local mixture fraction value Z will be analyzed (the dependency on Z is omitted for clarity):

$$S_d^{\mathrm{N}} = \frac{(\rho/\rho_u)\, S_d - S_L}{S_L} \tag{25}$$

In this equation, ρ_u denotes the density in the unburned gas that depends on the mixture fraction Z. The normalized deviation of the displacement speed from the laminar flame speed S_d^{N} takes a value of zero in a planar laminar flame, below a value of $S_d^{\mathrm{N}} = -1$ the displacement speed S_d is negative. The dependence of the flame displacement speed on the turbulent flame structure has been studied in numerous previous works [9, 13, 76, 79, 85, 90, 95, 96].

The PDFs of the normalized deviation of the displacement speed from the laminar flame speed conditioned on the progress of reaction and the height above the burner are given in Fig. 26. As observed for the PDFs of the normalized gradient difference $|\nabla Y_C|^{\mathrm{N}}$ discussed in the last section, the width of the PDFs of the normalized deviation of the displacement speed from the laminar flame

speed is also most narrow in the inner reaction zone and gets wider in the fresh and burned gas. The PDFs are less wide in the near region than in the far region, the peak values are slightly shifted towards negative values, most visible in the inner reaction zone, the burnout zone and in the burned gas. Especially in the far region, a certain amount of negative flame displacement speeds is found, indicated by values of the normalized displacement speed difference smaller than -1, a typical situation where this may occur is at the tip of a flame finger, i.e. at a point with strong positive curvature. This is due to the definition of the displacement speed that is an exact measure only for the movement of strictly parallel iso-surfaces, and has also been observed by others in simulations [13, 79, 87, 97] as well as in experiments [98].

The influence of the mean principal curvature and the normalized gradient difference, which have been discussed in the previous sections, on the normalized displacement speed difference is shown in Fig. 27. The mean principal curvature is negatively correlated with the normalized displacement speed difference, most significantly at the unburned side, in the preheat zone and in the reaction zone. The normalized gradient difference is positively correlated with the normalized displacement speed difference at the unburned side and in the preheat zone and negatively correlated at the burned side and in the burnout zone, however, no significant correlation exists in the reaction zone. In the unburned gas, the preheat zone and the reaction zone, the normalized displacement speed difference is most strongly correlated with the mean principal curvature. This reflects in the PDFs of the normalized displacement speed difference in Fig. 26, which are symmetric and bell-shaped at the unburned side and in the preheat zone and get narrower in the reaction zone. This observation is in agreement with the shape of the already discussed mean principal curvature PDFs in Fig. 21. In contrast, the normalized displacement speed difference is dominated by the negative correlation with the normalized gradient difference at the burned side and in the burnout zone. Therefore, the PDFs of the normalized displacement speed difference in Fig. 26 have long tails towards negative values and the peaks are shifted towards negative values at the burned side and in the burnout zone,

which is the inverse behavior as observed for the already discussed normalized gradient difference PDFs in Fig. 23.

To investigate the potential influence of the stratification (with the co-flow air) on the normalized displacement speed difference, the mixture fraction gradient normal to the flame was evaluated:

$$(\nabla Z)_n = n_i \frac{\partial Z}{\partial x_i} \tag{26}$$

The JPDFs of the normalized displacement speed difference with the mixture fraction gradient, which are presented in Fig. 27, show no significant correlation. It should be noted that the mixture fraction gradient is very small in magnitude compared to the progress variable gradient, which takes values up to around 630 m^{-1} in the laminar flame. Therefore, the stratification has no dominating influence on the flame propagation in the investigated case, which very likely will be different for the stratified setups of the burner, which have also been measured [24, 26].

To avoid the aforementioned occurrence of negative displacement speeds due to local changes in the flame thickness, the displacement speed might be averaged over the extracted flamelets (see Section 4), as discussed by Poinsot and Veynante [2]. Figure 28 presents the PDFs of the normalized deviation of the displacement speed of the flame (Eq. 24) averaged over the flamelets from the laminar flame speed averaged over the flamelets:

$$S_{df}^N = \frac{\left\langle \frac{\rho S_d}{\rho_u} \right\rangle_f - \langle S_L \rangle_f}{\langle S_L \rangle_f} \text{ with } \langle S \rangle_f = \frac{1}{L_f} \int_{C=0.01}^{C=0.99} S \, \mathrm{d}n \tag{27}$$

The PDFs of the normalized displacement speed difference integrated over the flamelet in Fig. 28 are less wide and symmetric than the instantaneous ones in Fig. 26. This demonstrates again that many of the observed effects are due to the formulation of the displacement speed. However, the PDFs are still relatively broad and a small amount of slightly negative values of the displacement speed (corresponding to normalized displacement speed difference smaller than -1) still can occur in the far region, implying that the mean principal curvature

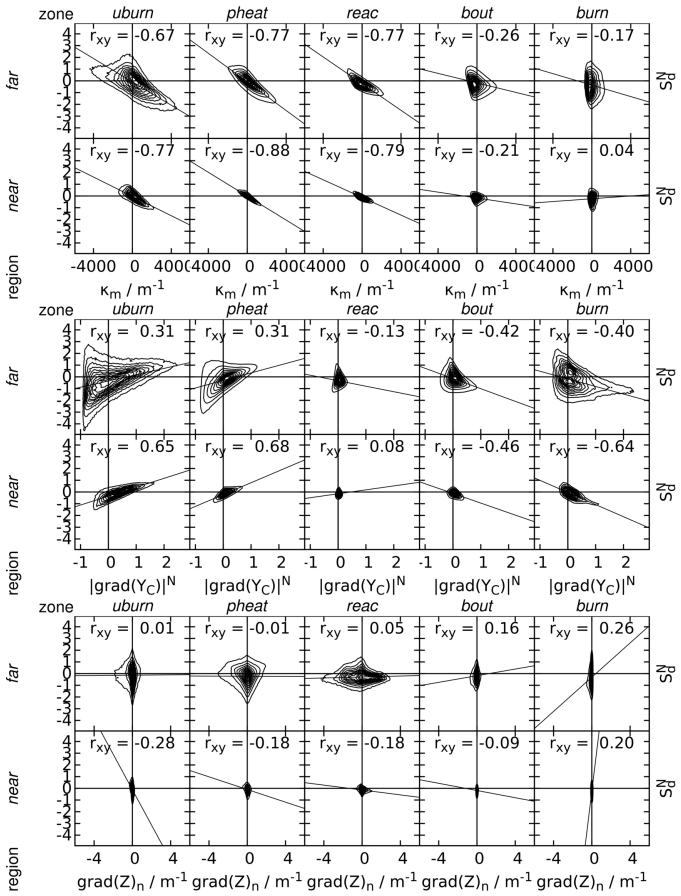

Figure 27: Conditioned joint PDFs of the normalized deviation of the displacement speed of the flame front from the laminar flame speed (see Eq. 25) as a function of the mean principal curvature of the flame front (top, see Eq. 21), the normalized gradient difference of the turbulent and the laminar flame (middle, see Eq. 22) and the mixture fraction gradient normal to the flame (bottom, see Eq. 26). *The different plots represent the conditioning on increasing height above the burner from bottom to top and increasing progress of the reaction from left to right (see Section 4). The Pearson correlation coefficients* r_{xy} *and linear regression lines are also given.*

is strongly positive. This corresponds to flamelets in regions where a burned mixture pocket penetrates deeply into the fresh gas. This is in discordance with the observations of Hilka [2], who found no negative values for the integrated displacement speed in a canonical flame configuration.

The flame speed definition that is most insensitive against curvature effects is the integrated consumption speed over the flamelet, in this work the normalized deviation from the laminar flame speed is considered:

$$S_c^N = \frac{S_c - \langle S_L \rangle_f}{\langle S_L \rangle_f} \text{ with } S_c = \frac{1}{\rho_u Y_{\mathrm{C},b}} \int_{C=0.01}^{C=0.99} \dot{\omega}_{\mathrm{C}} \, dn \tag{28}$$

In this equation, $Y_{\mathrm{C},b}$ denotes the progress variable value at the burned side of the flame that depends on the mixture fraction Z. The PDFs of the normalized consumption speed difference in Fig. 28 are much less wide than the ones for the normalized displacement speed difference, no negative values of the consumption speed occur (which would correspond to a normalized consumption speed difference smaller than -1). The absence of negative values follows from the definition of the consumption speed as the integral of reaction source term over the flame, which is always positive. In the far region, the PDF has a long tail towards positive values, which can be attributed to stratification effects, as already observed and discussed for the integrated progress variable source term in C-space shown in Fig. 5. Similar shapes of the consumption speed PDFs for a canonical configuration have also been reported by Dunstan et al. [90].

To find out to which extent the normalized displacement speed difference is a measure for the normalized consumption speed difference, the left two plots in Fig. 29 present the related JPDFs. It becomes clear that there is basically no correlation at all between the two quantities. When only the sum of displacement speed due to flame normal diffusion and reaction $S_n + S_r$ is considered, as in the right two plots of Fig. 29, a significant correlation is achieved for the flamelets in the near region. For the flamelets in the far region there is still a clear correlation, but it is much weaker and gets very broad especially towards higher normalized consumption speed difference values. This makes the sum of

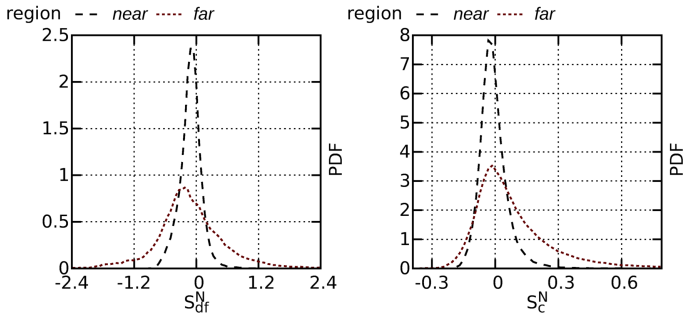

Figure 28: Conditioned PDFs of the flamelet-averaged value of the normalized deviation of the displacement speed of the flame front from the laminar flame speed (left, Eq. 27) and the normalized deviation of the flamelet-integrated consumption speed (right, see Eq. 28) from the laminar flame speed. *The different lines represent the conditioning on the height above the burner (see Section 4).*

the flame displacement speed only due to flame normal diffusion and reaction a better, but still not an ideal measure for the flame consumption speed.

7. Conclusions

An unsteady simulation of a lab-scale turbulent premixed flame experiment was presented, where the combustion process was modeled with the premixed flamelet generated manifold (PGFM) chemistry tabulation approach. It has been demonstrated that the applied grid resolution of 100 µm was indeed sufficient to resolve the flame without any sub-filter modeling and all velocity scales inside and in the vicinity of the flame region. Only on the unburned side of the flame, a small amount of unresolved velocity scales was present, which were modeled by the σ-model. A good agreement between experiment and simulation was found for mean and rms profiles.

The results were analyzed in detail with ensemble-averaged and flamelet-averaged PDFs, JPDFs and conditional means. It was found that the analysis needs to be carried out separately for the regions near and far from the burner exit, due to the different turbulence levels in the two inlet streams and the additional turbulence produced in the shear layer between the streams. Furthermore,

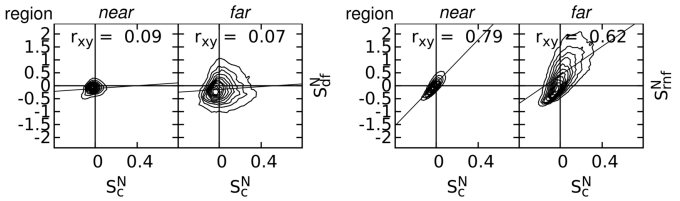

Figure 29: Conditioned joint PDFs of the flamelet-averaged value of the normalized deviation of the displacement speed of the flame front from the laminar flame speed (left two plots, see Eq. 25) and the flamelet-averaged value of the normalized deviation of the displacement speed of the flame front only due to flame normal diffusion and reaction $S_n + S_r$ from the laminar flame speed (right two plot) as a function of the normalized deviation of the flamelet-integrated consumption speed (right, see Eq. 28) from the laminar flame speed. *The different plots represent the conditioning on increasing height above the burner from left to right (see Section 4). The Pearson correlation coefficients* $\mathrm{r_{xy}}$ *and linear regression lines are also given.*

the location of the combustion process in the regime diagram depends on the progress of the reaction, as a large amount of the turbulent fluctuations were dissipated inside the flame.

A skewness towards negative values was found for the PDFs of the flame normal strain rate component, which could be attributed mainly to the mean flow configuration in the near region and mainly to turbulent fluctuations in the far region. The latter was due to a preferential alignment of the most compressive principal strain rate eigenvector with the flame normal direction, which became stronger at the burned side of the flame compared to the unburned side. It was demonstrated that this stronger alignment was mainly caused by a change of the most compressive principal strain rate eigenvector direction. The compressive strain was reduced with increasing progress of reaction.

The distribution of the mean principal curvature was broad and symmetric in the unburned gas, with increasing progress of reaction it became narrower and skewed towards positive values. This skewness could be attributed to the reduction of the compressive strain with increasing progress of reaction.

The magnitude of the progress variable gradient was close to the laminar flame value in the inner reaction zone and varied over a broad range at the

unburned and burned side of the flame. The flame structure was slightly thinner than the laminar one except on the unburned side of the flame in the far region, where it was thicker. The thinning could be attributed to the predominantly compressive strain, the thickening to flame speed variations caused by the reduction of mean principal curvature. The deviation of the reaction zones from a straight line was determined by the tortuosity of the extracted turbulent flamelets, it was found that nearly straight flamelets were most likely in the near region, whereas the flamelets were more strongly folded in the far region.

The flame displacement speed showed a relatively broad distribution that was slightly shifted towards smaller values especially in the far region and the burned gas, where also negative values occurred. It was demonstrated that the flame displacement speed was mainly influenced by the mean principal curvature in the fresh gas, the preheat zone and the inner reaction zone. In contrast, in the burnout region and in the burned gas the flame displacement speed was dominated by the gradient of the progress variable field. The flame displacement speed was also averaged over the flamelets, it was demonstrated that it is hardly correlated with the integrated consumption speed over the flamelets. A more significant correlation was found between the consumption speed and the displacement speed due to reaction and flame normal diffusion component.

To the best of our knowledge, this is the first time that such detailed Direct Numerical Simulation (DNS) analysis was performed for a flame resolved simulation dataset, which has been extensively validated against experimental measurements. Overall, the present paper confirms many findings from DNS of simpler configurations and thereby demonstrates that these findings can be translated to real turbulent flames, for which experimental validation data is available.

The flame resolved simulation database used in this paper is available to other researchers, respective queries can be addressed to the Chair of Fluid Dynamics of the University of Duisburg-Essen [99].

8. Acknowledgements

The authors gratefully acknowledge the funding from the state of North Rhine-Westphalia and the compute time granted on JUQUEEN at Jülich Supercomputing Centre (JSC), through the John von Neumann Institute for Computing (NIC). We also would like to thank Vincent Moureau and Martin Rieth for valuable discussions.

References

[1] J. H. Chen, Petascale direct numerical simulation of turbulent combustion - fundamental insights towards predictive models, Proc. Combust. Inst. 33 (2011) 99–123.

[2] T. Poinsot, D. Veynante, Theoretical and Numerical Combustion, Aquaprint, Bordeaux, France, 3rd edn., 2012.

[3] A. Trouvé, T. Poinsot, The evolution equation for the flame surface density in turbulent premixed combustion, J. Fluid Mech. 278 (1994) 1–31.

[4] C. J. Rutland, R. S. Cant, Turbulent transport in premixed flames, Proceedings of the Summer Programm, Center for Turbulence Research, Stanford (1994) 75–94.

[5] T. Poinsot, S. Candel, A. Trouvé, Applications of Direct Numerical Simulation to premixed turbulent combustion, Prog. Energ. Combust. 21 (1996) 531–576.

[6] S. Nishiki, T. Hasegawa, R. Borghi, R. Himeno, Modeling of flame-generated turbulence based on direct numerical simulation databases, Proc. Combust. Inst. 29 (2) (2002) 2017 – 2022.

[7] P. Domingo, L. Vervisch, S. Payet, R. Hauguel, DNS of a premixed turbulent V flame and LES of a ducted flame using a FSD-PDF subgrid scale closure with FPI-tabulated chemistry, Combust. Flame 143 (2005) 566–586.

[8] J. A. van Oijen, R. J. M. Bastiaans, G. R. A. Groot, L. P. H. De Goey, Direct Numerical Simulations of Premixed Turbulent Flames with Reduced Chemistry: Validation and Flamelet Analysis, Flow Turbul. Combust. 75 (1-4) (2005) 67–84.

[9] N. Chakraborty, M. Klein, R. S. Cant, Stretch rate effects on displacement speed in turbulent premixed flame kernels in the thin reaction zones regime, Proc. Combust. Inst. 31 (1) (2007) 1385–1392.

[10] N. Chakraborty, R. S. Cant, Direct Numerical Simulation analysis of the Flame Surface Density transport equation in the context of Large Eddy Simulation, Proc. Combust. Inst. 32 (1) (2009) 1445 – 1453.

[11] E. R. Hawkes, J. H. Chen, Comparison of direct numerical simulation of lean premixed methaneair flames with strained laminar flame calculations, Combust. Flame 144 (12) (2006) 112 – 125.

[12] A. Gruber, E. R. Hawkes, J. H. Chen, R. Sankaran, Turbulent flame-wall interaction: a direct numerical simulation study, J. Fluid Mech. 658 (2010) 5–32.

[13] Z. M. Nikolaou, N. Swaminathan, Direct Numerical Simulation of Complex Fuel Combustion with Detailed Chemistry: Physical Insight and Mean Reaction Rate Modeling, Combust. Sci. Technol. 187 (11) (2015) 1759–1789.

[14] A. J. Aspden, M. S. Day, J. B. Bell, Three-dimensional direct numerical simulation of turbulent lean premixed methane combustion with detailed kinetics, Combust. Flame 166 (2016) 266 – 283.

[15] R. Sankaran, E. R. Hawkes, J. H. Chen, T. Lu, C. K. Law, Structure of a spatially developing turbulent lean methaneair Bunsen flame, Proc. Combust. Inst. 31 (1) (2007) 1291 – 1298.

[16] R. Sankaran, E. R. Hawkes, C. S. Yoo, J. H. Chen, Response of flame thickness and propagation speed under intense turbulence in spatially developing

lean premixed methaneair jet flames, Combust. Flame 162 (9) (2015) 3294 – 3306.

[17] J. H. Bell, M. S. Day, J. F. Grcar, M. J. Lijewski, J. F. Driscoll, S. A. Filatyev, Numerical simulation of a laboratory-scale turbulent slot flame, Proc. Combust. Inst. 31 (1) (2007) 1299–1307.

[18] A. W. Vreman, J. A. van Oijen, L. P. H. de Goey, R. J. M. Bastiaans, Direct numerical simulation of hydrogen addition in turbulent premixed Bunsen flames using flamelet-generated manifold reduction, Int. J. Hydrogen Energ. 34 (6) (2009) 2778 – 2788.

[19] E. S. Richardson, R. Sankaran, R. W. Grout, J. H. Chen, Numerical analysis of reactiondiffusion effects on species mixing rates in turbulent premixed methaneair combustion, Combust. Flame 157 (3) (2010) 506 – 515.

[20] P. Moin, K. Mahesh, Direct numerical simulation: A tool in turbulence research, Annu. Rev. Fluid Mech. 30 (1998) 539–578.

[21] J. Kim, P. Moin, R. Moser, Turbulence statistics in fully developed channel flow at low Reynolds number, J. Fluid Mech. 177 (1987) 133–166.

[22] V. Moureau, P. Domingo, L. Vervisch, From Large-Eddy Simulation to Direct Numerical Simulation of a lean premixed swirl flame: Filtered laminar flame-PDF modeling, Combust. Flame 158 (7) (2011) 1340 – 1357.

[23] W. Meier, P. Weigand, X. R. Duan, R. Giezendanner-Thoben, Detailed characterization of the dynamics of thermoacoustic pulsations in a lean premixed swirl flame, Combust. Flame 150 (12) (2007) 2 – 26.

[24] M. S. Sweeney, S. Hochgreb, M. J. Dunn, R. S. Barlow, The structure of turbulent stratified and premixed methane/air flames I: Non-swirling flows, Combust. Flame 159 (9) (2012) 2896 – 2911.

[25] M. S. Sweeney, S. Hochgreb, M. J. Dunn, R. S. Barlow, The structure of turbulent stratified and premixed methane/air flames II: Swirling flows, Combust. Flame 159 (9) (2012) 2912 – 2929.

[26] R. Zhou, S. Balusamy, M. S. Sweeney, R. S. Barlow, S. Hochgreb, Flow field measurements of a series of turbulent premixed and stratified methane/air flames, Combust. Flame 160 (10) (2013) 2017 – 2028.

[27] M. Euler, R. Zhou, S. Hochgreb, A. Dreizler, Temperature measurements of the bluff body surface of a Swirl Burner using phosphor thermometry, Combust. Flame 161 (11) (2014) 2842 – 2848.

[28] M. M. Kamal, R. Zhou, S. Balusamy, S. Hochgreb, Favre- and Reynolds-averaged velocity measurements: Interpreting PIV and LDA measurements in combustion, Proc. Combust. Inst. 35 (3) (2015) 3803 – 3811.

[29] M. M. Kamal, R. S. Barlow, S. Hochgreb, Conditional analysis of turbulent premixed and stratified flames on local equivalence ratio and progress of reaction, Combust. Flame (2015) 10.1016/j.combustflame.2015.07.026.

[30] S. Nambully, P. Domingo, V. Moureau, L. Vervisch, A filtered-laminar-flame PDF sub-grid scale closure for LES of premixed turbulent flames. Part I: Formalism and application to a bluff-body burner with differential diffusion, Combust. Flame 161 (7) (2014) 1756–1774.

[31] S. Nambully, P. Domingo, V. Moureau, L. Vervisch, A filtered-laminar-flame PDF sub-grid-scale closure for LES of premixed turbulent flames: II. Application to a stratified bluff-body burner, Combust. Flame 161 (7) (2014) 1775–1791.

[32] F. Proch, A. M. Kempf, Numerical analysis of the Cambridge stratified flame series using artificial thickened flame LES with tabulated premixed flame chemistry, Combust. Flame 161 (10) (2014) 2627 – 2646.

[33] R. Mercier, T. Schmitt, D. Veynante, B. Fiorina, The influence of combustion SGS submodels on the resolved flame propagation. Application to the LES of the Cambridge stratified flames, Proc. Combust. Inst. 35 (2) (2015) 1259 – 1267.

[34] T. Brauner, W. P. Jones, A. J. Marquis, LES of the Cambridge Stratified Swirl Burner using a Sub-grid pdf Approach, Flow Turbul. Combust. (2016) 1–21.

[35] F. Proch, P. Domingo, L. Vervisch, A. M. Kempf, Flame resolved simulation of a turbulent premixed bluff-body burner experiment. Part II: A-priori and a-posteriori investigation of sub-grid scale wrinkling closures in the context of artificially thickened flame modeling, Combust. Flame (under review) –.

[36] U. Maas, S. B. Pope, Simplifying chemical kinetics: Intrinsic low-dimensional manifolds in composition space, Combust. Flame 88 (34) (1992) 239 – 264.

[37] O. Gicquel, N. Darabiha, D. Thévenin, Liminar premixed hydrogen/air counterflow flame simulations using flame prolongation of ILDM with differential diffusion, Proc. Combust. Inst. 28 (2) (2000) 1901 – 1908.

[38] B. Fiorina, O. Gicquel, L. Vervisch, S. Carpentier, N. Darabiha, Approximating the chemical structure of partially premixed and diffusion counterflow flames using FPI flamelet tabulation, Combust. Flame 140 (3) (2005) 147 – 160.

[39] P.-D. Nguyen, L. Vervisch, V. Subramanian, P. Domingo, Multidimensional flamelet-generated manifolds for partially premixed combustion, Combust. Flame 157 (1) (2010) 43–61.

[40] J. A. van Oijen, L. P. H. de Goey, Modelling of Premixed Laminar Flames using Flamelet-Generated Manifolds, Combust. Sci. Technol. 161 (1) (2000) 113–137.

[41] J. A. van Oijen, R. J. M. Bastiaans, L. P. H. de Goey, Low-dimensional manifolds in direct numerical simulations of premixed turbulent flames, Proc. Combust. Inst. 31 (1) (2007) 1377–1384.

[42] D. G. Goodwin, Cantera, http://code.google.com/p/cantera, 2009.

[43] G. P. Smith, D. M. Golden, M. Frenklach, N. W. Moriarty, B. Eiteneer, M. Goldenberg, C. T. Bowman, R. K. Hanson, S. Song, W. C. Gardiner, Jr., V. V. Lissianski, Z. Qin, http://www.me.berkeley.edu/gri_mech, 2000.

[44] M. Ihme, L. Shunn, J. Zhang, Regularization of reaction progress variable for application to flamelet-based combustion models, J. Comput. Phys. 231 (23) (2012) 7715 – 7721.

[45] Y.-S. Niu, L. Vervisch, P. D. Tao, An optimization-based approach to detailed chemistry tabulation: Automated progress variable definition, Combust. Flame 160 (4) (2013) 776 – 785.

[46] U. Prüfert, S. Hartl, F. Hunger, D. Messig, M. Eiermann, C. Hasse, A Constrained Control Approach for the Automated Choice of an Optimal Progress Variable for Chemistry Tabulation, Flow Turbul. Combust. 94 (3) (2015) 593–617.

[47] R. W. Bilger, S. H. Stårner, R. J. Kee, On reduced mechanisms for methane-air combustion in nonpremixed flames, Combust. Flame 80 (2) (1990) 135 – 149.

[48] F. Nicoud, H. B. Toda, O. Cabrit, S. Bose, J. Lee, Using singular values to build a subgrid-scale model for large eddy simulations, Phys. Fluids 23 (8) (2011) 085106.

[49] M. Boger, D. Veynante, H. Boughanem, A. Trouve, Direct numerical simulation analysis of flame surface density concept for large eddy simulation of turbulent premixed combustion, Proc. Combust. Inst. 27 (1) (1998) 917 – 925.

[50] H. Pitsch, H. Steiner, Large-eddy simulation of a turbulent piloted methane/air diffusion flame (Sandia flame D), Phys. Fluids 12 (10) (2000) 2541–2554.

[51] B. Fiorina, R. Vicquelin, P. Auzillon, N. Darabiha, O. Gicquel, D. Veynante, A filtered tabulated chemistry model for LES of premixed combustion, Combust. Flame 157 (3) (2010) 465 – 475.

[52] G. Kuenne, F. Seffrin, F. Fuest, T. Stahler, A. Ketelheun, D. Geyer, J. Janicka, A. Dreizler, Experimental and numerical analysis of a lean premixed stratified burner using 1D Raman/Rayleigh scattering and large eddy simulation, Combust. Flame 159 (8) (2012) 2669 – 2689.

[53] M. Klein, A. Sadiki, J. Janicka, A digital filter based generation of inflow data for spatially developing direct numerical or large eddy simulations, J. Comput. Phys. 186 (2003) 652–665.

[54] A. M. Kempf, S. Wysocki, M. Pettit, An Efficient, Parallel Low-Storage Implementation of Klein's Turbulence Generator for LES and DNS, Comput. Fluids 60 (2012) 58–60.

[55] A. M. Kempf, B. Geurts, J. C. Oefelein, Error Analysis of Large-Eddy Simulation of the Turbulent Non-premixed Sydney Bluff-Body Flame, Combust. Flame 158 (2011) 2408–2419.

[56] F. Proch, A. M. Kempf, Modeling heat loss effects in the large eddy simulation of a model gas turbine combustor with premixed flamelet generated manifolds, Proc. Combust. Inst. 35 (3) (2015) 3337 – 3345.

[57] M. Rieth, F. Proch, O. T. Stein, M. W. A. Pettit, A. M. Kempf, Comparison of the Sigma and Smagorinsky LES models for grid generated turbulence and a channel flow, Comput. Fluids 99 (0) (2014) 172 – 181.

[58] M. Rabaçal, B. M. Franchetti, F. C. Marincola, F. Proch, M. Costa, C. Hasse, A. M. Kempf, Large Eddy Simulation of coal combustion in a large-scale laboratory furnace, Proc. Combust. Inst. 35 (3) (2015) 3609 – 3617.

[59] A. Rittler, F. Proch, A. M. Kempf, LES of the Sydney piloted spray flame series with the PFGM/ATF approach and different sub-filter models, Combust. Flame 162 (4) (2015) 1575 – 1598.

[60] G. Zhou, Numerical simulations of physical discontinuities in single and multi-fluid flows for arbitrary Mach numbers, Ph.D. thesis, Chalmers University of Technology, Goteborg, Sweden, 1995.

[61] N. Peters, Turbulent Combustion, Cambridge University Press, 2000.

[62] S. B. Pope, Turbulent Flows, Cambridge University Press, 2000.

[63] K. N. C. Bray, The Challenge of turbulent combustion, Proc. Combust. Inst. 26 (1996) 1–26.

[64] A. P. D. Cruz, A. M. Dean, J. M. Grenda, A numerical study of the laminar flame speed of stratified methane/air flames, Proc. Combust. Inst. 28 (2) (2000) 1925 – 1932.

[65] R. S. Barlow, M. J. Dunn, M. S. Sweeney, S. Hochgreb, Effects of preferential transport in turbulent bluff-body-stabilized lean premixed CH4/air flames, Combust. Flame 159 (8) (2012) 2563 – 2575.

[66] R. Mercier, B. Fiorina, F. Proch, A. M. Kempf, Numerical and modeling strategies for the simulation of the Cambridge stratified flame series, in: TSFP digital library online, Begel House Inc., 2013.

[67] F. Proch, M. W. A. Pettit, T. Ma, M. Rieth, A. M. Kempf, Direct and Large-Eddy Simulation IX, chap. Investigations on the Effect of Different Subgrid Models on the Quality of LES Results, Springer International Publishing, Cham, ISBN 978-3-319-14448-1, 141–147, 2015.

[68] J. Bell, M. Day, J. Grcar, M. Lijewski, Active control for statistically stationary turbulent premixed flame simulations, Comm. App. Math. Comp. Sci. 1 (1) (2007) 29–51.

[69] A. Y. Poludnenko, E. S. Oran, The interaction of high-speed turbulence with flames: Global properties and internal flame structure, Combust. Flame 157 (5) (2010) 995 – 1011.

[70] A. Y. Poludnenko, E. S. Oran, The interaction of high-speed turbulence with flames: Turbulent flame speed, Combust. Flame 158 (2) (2011) 301 – 326.

[71] A. N. Lipatnikov, J. Chomiak, V. A. Sabelnikov, S. Nishiki, T. Hasegawa, Unburned mixture fingers in premixed turbulent flames, Proc. Combust. Inst. 35 (2) (2015) 1401 – 1408.

[72] R. Borghi, Turbulent combustion modelling, Prog. Energy Combust. Sci. 14 (1988) 245–292.

[73] W. T. Ashurst, N. Peters, M. D. Smooke, Numerical Simulation of Turbulent Flame Structure with Non-unity Lewis Number, Combust. Sci. Technol. 53 (4-6) (1987) 339–375.

[74] D. C. Haworth, T. J. Poinsot, Numerical simulations of Lewis number effects in turbulent premixed flames, J. Fluid Mech. 244 (1992) 405–436.

[75] C. J. Rutland, A. Trouvé, Direct simulations of premixed turbulent flames with nonunity Lewis numbers, Combust. Flame 94 (12) (1993) 41 – 57.

[76] N. Chakraborty, R. S. Cant, Influence of Lewis number on curvature effects in turbulent premixed flame propagation in the thin reaction zones regime, Phys. Fluids 17 (10) (2005) 105105/1–105105/20.

[77] L. Cifuentes, C. Dopazo, J. Martin, P. Domingo, L. Vervisch, Local volumetric dilatation rate and scalar geometries in a premixed methane-air turbulent jet flame, Proc. Combust. Inst. 35 (2015) 1295–1303.

[78] A. Amato, M. Day, R. K. Cheng, J. Bell, D. Dasgupta, T. Lieuwen, Topology and burning rates of turbulent, lean, H2/air flames, Combust. Flame 162 (12) (2015) 4553 – 4565.

[79] N. Chakraborty, N. Swaminathan, Influence of the Damköhler number on turbulence-scalar interaction in premixed flames. I. Physical insight, Phys. Fluids 19 (4) (2007) 045103.

[80] N. Chakraborty, Comparison of displacement speed statistics of turbulent premixed flames in the regimes representing combustion in corrugated flamelets and thin reaction zones, Phys. Fluids 19 (10) (2007) 105109.

[81] G. Hartung, J. Hult, C. F. Kaminski, J. W. Rogerson, N. Swaminathan, Effect of heat release on turbulence and scalar-turbulence interaction in premixed combustion, Phys. Fluids 20 (3) (2008) 035110.

[82] A. M. Steinberg, J. F. Driscoll, N. Swaminathan, Statistics and dynamics of turbulenceflame alignment in premixed combustion, Combust. Flame 159 (8) (2012) 2576 – 2588.

[83] T. Sponfeldner, I. Boxx, F. Beyrau, Y. Hardalupas, W. Meier, A. M. K. P. Taylor, On the alignment of fluid-dynamic principal strain-rates with the 3D flamelet-normal in a premixed turbulent V-flame, Proc. Combust. Inst. 35 (2) (2015) 1269 – 1276.

[84] H. Pitsch, H. Steiner, Scalar mixing and dissipation rate in Large-Eddy Simulations of non-premixed turbulent combustion, Proc. Combust. Inst. 28 (2000) 41–49.

[85] T. Echekki, J. H. Chen, Unsteady strain rate and curvature effects in turbulent premixed methane-air flames, Combust. Flame 106 (12) (1996) 184 – 202.

[86] M. Tanahashi, M. Fujimura, T. Miyauchi, Coherent fine-scale eddies in turbulent premixed flames, Proc. Combust. Inst. 28 (1) (2000) 529 – 535.

[87] N. Chakraborty, S. Cant, Unsteady effects of strain rate and curvature on turbulent premixed flames in an inflowoutflow configuration, Combust. Flame 137 (12) (2004) 129 – 147.

[88] N. Chakraborty, R. S. Cant, Influence of Lewis number on strain rate effects in turbulent premixed flame propagation, Int. J. Heat Mass Tran. 49 (1314) (2006) 2158 – 2172.

[89] M. Klein, N. Chakraborty, K. W. Jenkins, R. S. Cant, Effects of initial radius on the propagation of premixed flame kernels in a turbulent environment, Phys. Fluids 18 (5) (2006) 055102.

[90] T. D. Dunstan, N. Swaminathan, K. N. C. Bray, Influence of flame geometry on turbulent premixed flame propagation: a DNS investigation, J. Fluid Mech. 709 (2012) 191–222.

[91] N. Chakraborty, R. S. Cant, Effects of strain rate and curvature on surface density function transport in turbulent premixed flames in the thin reaction zones regime, Phys. Fluids 17 (6) (2005) 065108.

[92] C. H. Gibson, Fine Structure of Scalar Fields Mixed by Turbulence. I. ZeroGradient Points and Minimal Gradient Surfaces, Phys. Fluids 11 (11) (1968) 2305–2315.

[93] S. B. Pope, The evolution of surfaces in turbulence, Int. J. Eng. Sci. 26 (5) (1988) 445 – 469.

[94] T. Echekki, J. H. Chen, Analysis of the contribution of curvature to premixed flame propagation, Combust. Flame 118 (12) (1999) 308 – 311.

[95] N. Peters, The turbulent burning velocity for large-scale and small-scale turbulence, J. Fluid Mech. 384 (1999) 107–132.

[96] M. Klein, N. Chakraborty, R. S. Cant, Effects of Turbulence on Self-sustained Combustion in Premixed Flame Kernels: A Direct Numerical Simulation (DNS) Study, Flow Turbul. Combust. 81 (4) (2008) 583–607.

[97] I. R. Gran, T. Echekki, J. H. Chen, Negative flame speed in an unsteady 2-D premixed flame: A computational study, Proc. Combust. Inst. 26 (1) (1996) 323 – 329.

[98] B. Peterson, E. Baum, B. Böhm, A. Dreizler, Early flame propagation in a spark-ignition engine measured with quasi 4D-diagnostics, Proc. Combust. Inst. 35 (3) (2015) 3829 – 3837.

[99] A. M. Kempf, F. Proch, https://www.uni-due.de/ivg/fluiddynamik/, 2016.